

Texas Active Target (TexAT) Detector for Experiments With Rare Isotope Beams

E. Koshchiy^a, G.V. Rogachev^{a,b}, E. Pollacco^c, S. Ahn^a, E. Uberseder^a, J. Hooker^{a,b,1}, J. Bishop^{a,b}, E. Aboud^{a,b}, M. Barbui^a, V.Z. Goldberg^a, C. Hunt^{a,b}, H. Jayatissa^{a,b}, C. Magana^{a,b}, R. O'Dwyer^{a,b}, B.T. Roeder^a, A. Saastamoinen^a, S. Upadhyayula^{a,b}

^aCyclotron Institute, Texas A&M University, College Station, TX 77843, USA

^bDepartment of Physics & Astronomy, Texas A&M University, College Station, TX 77843, USA

^cIRFU, CEA, Saclay, Gif-Sur-Ivette, France

Abstract

The TexAT (Texas Active Target) detector is a new active-target time projection chamber (TPC) that was built at the Cyclotron Institute Texas A&M University. The detector is designed to be of general use for nuclear structure and nuclear astrophysics experiments with rare isotope beams. TexAT combines a highly segmented Time Projection Chamber (TPC) with two layers of solid state detectors. It provides high efficiency and flexibility for experiments with low intensity exotic beams, allowing for the 3D track reconstruction of the incoming and outgoing particles involved in nuclear reactions and decays.

PACS 29.40.Cs Gas-filled counters: ionization chambers, proportional, and avalanche counters; 29.40.Gx Tracking and position-sensitive detectors

Keywords: Active gas target; Inverse kinematics; Time projection chambers; Charged particle detection; Micromegas detector; Silicon-strip detectors; CsI(Tl) detectors; Radioactive beams; Particle track; Vertex reconstruction

1. Introduction

Over the last 20-30 years, experiments with rare isotope beams (RIBs) developed from being exotic undertakings in a select few laboratories into the main stream of nuclear science. RIBs provide a pathway to venture far beyond the constraints typically encountered in experiments with stable beams. RIBs open up an opportunity to study very exotic nuclei using relatively simple and well understood reactions, such as elastic and inelastic scattering, one/two nucleon transfer, Coulomb excitation, etc. They allow key reaction rates to be measured that are relevant for explosive processes in astrophysics with radioactive nuclei. All these benefits come at a price. The typical intensity of RIBs is many orders of magnitude lower than that of stable beams. Therefore, efficiency of the experimental setup becomes the determining factor for RIBs experiments. One of the most efficient experimental approaches that can be used with RIBs is utilizing an active target detector. These detectors can be designed to have almost 4π solid angle coverage, and they naturally allow the use of thick targets without loss of energy resolution. Thick targets also allows the measurement of excitation functions without the need to change the beam energy [1]. The versatility of these devices for RIB experiments has been recognized and many nuclear physics laboratories around the world are in the process of constructing and using the general purpose devices (TACTIC at U of York/TRIUMF [2], MAYA at GANIL/TRIUMF [3], AT-TPC at NSCL [4], ACTAR

at GANIL/GSI [5], ANASEN at FSU/LSU/NSCL [6], MUSIC [7], MSTPC [8] and others). Some TPCs aimed at specific processes e.g., $2p$ - decay [9], or the only optical readout active target TPC for studies with gamma-ray beams [10]. A comprehensive overview on the subject can be found in [11], [12], [13].

While the concept is similar for all active target detectors (the target material is spatially extended and “active” to allow for tracking of the reaction products), the specific implementation may be very different depending on the energy range, type and quality of RIBs characteristic of the particular facility. We designed and constructed a general-purpose active target detector (Texas Active Target, TexAT) aimed at low energy nuclear physics experiments with rare isotope beams produced by either the MARS recoil separator [14], or the new reaccelerated beam facility currently under development at the Cyclotron Institute Texas A&M University. TexAT can be used for a wide variety of experiments to detect the charged products of nuclear reactions with rare isotope beams. In an “active” target mode, the nuclei from the detector gas mixture act as a target. Resonant elastic and inelastic scattering of protons and α -particles, (α,p) and (p,α) reactions, nucleon-transfer reactions, such as (d,p), ($d,^3\text{He}$), (p,d), (p,t), (α,t), as well as a fusion-evaporation reactions are examples of the experiments that can be performed with TexAT. TexAT can also be used for β -delayed charged particle emission experiments with beams of radioactive ions.

2. Overview of TexAT design and main components

2.1. General design

TexAT consists of a gas-filled Time Projection Chamber (TPC) and two layers of solid states detectors which surround

Email addresses: koshchiy@tamu.edu (E. Koshchiy), rogachev@tamu.edu (G.V. Rogachev)

¹Present address: Department of Physics and Astronomy, University of Tennessee, Knoxville, Tennessee 37996, USA

the TPC in Cartesian geometry.

TPCs with a high level of segmentation in the readout plane provide 3D- vertex and tracking capabilities for both incoming beam ions and charged reaction products and allows for information on the energy losses for each track in the gas.

Solid state detectors contribute an additional particle ID and the total energy information for the ions that escape the gas volume. TexAT has been designed to be able to operate in a rather broad energy range: from sub-MeV to tens MeV/nucleon and for some experiments the energy of protons can be as high as ~ 100 MeV.

The typical thickness of high-quality transient Si detectors available on the market is about 1 mm. They have been used to form an inner (ΔE)- layer of the solid- state detector wall.

To stop the light ions with energies greater than the punch-through energies for the Si detectors, a thick detector is required. When choosing the total absorption detectors we focused on using commercially available and affordable thick detectors of large area. Currently, the thickest semiconductor detectors for charged particles are manufactured using the so called lithium-drift technology. For example, 30 mm in diameter, 12 mm thick coaxial type Si(Li)- detector for charged particle detection have been manufactured and investigated in [15].

Still, large (50mm x 50mm) Si(Li)- detectors of the required thickness (~ 10 mm) are very expensive and require special care. Moreover, in some of the experiments envisioned with TexAT, protons with energies as high as 50 MeV may need to be detected. Even 10 mm Si would not be sufficient for these applications. An additional consideration is that CsI(Tl) scintillators are efficient γ - detectors, that can be used in experiments that require charged particle- γ coincidence with TexAT. Therefore, for both practical and scientific reasons we have decided to use the 40 mm thick scintillation CsI(Tl) to form the outer wall backing Si detectors.

The 3D-rendered representation of TexAT is shown in Fig.1. In the full configuration, the TPC is surrounded by an array of 58 Si-CsI(Tl) telescope detectors: 8 at the “upstream”/“beam” - side, 10 at the “downstream” - and both “beam- left” and “beam- right”- sides (30 total) and 20 at the “bottom” - of TPC side (shown on top in Fig. 1).

The length of the active area of TPC is 224 mm, an active volume is about $5,000 \text{ cm}^3$, and the total solid angle covered by Si-CsI(Tl) telescopes is about 3π , providing high efficiency for experiments with low intensity exotic beams. The detailed description of individual components is provided below.

2.1.1. Time Projection Chamber

The two main components of the TexAT TPC are the Micromegas detector and a field cage.

The key element is the Micromegas (Micro-MEsh Gaseous Structures) detector [16, 17]. It consists of a highly segmented anode readout board with a woven stainless steel mesh stretched above it. Such geometry creates a parallel- plate gas- electron amplification volume, where the primary electrons, generated by ionization in the active “drift” volume of the detector are amplified. It is basically an “ideal” parallel- plate gas-electron proportional counter, where the micro-mesh side is rendered

Detectors: Si (58 total);
CsI(Tl) (58 total);
Micromegas: 1024 channels

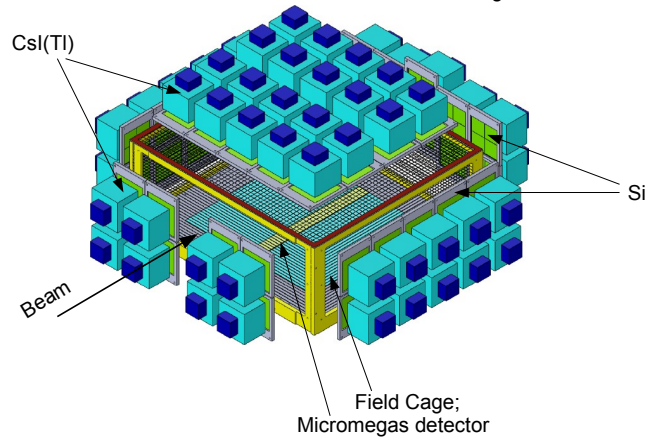


Figure 1: Sketch of the TexAT Assembly. Detailed description of the individual components is provided in the text.

approximately 95% transparent to electrons. This is because the field between the micromesh and the readout plane is of the order of 30 kV/cm and considerably higher than the drift field above the mesh. A field cage provides a uniform electric field in the active volume of a TPC. To ensure an operation in drift mode a reduced field strength value E/P has to be smaller than 20 V/cm/Torr (see, for example [18]). For all of the experiments performed with TexAT the reduced field strength is between 0.05 V/cm/Torr and 5 V/cm/Torr .

A detailed description of the field cage is given in Sec. 2.2.

The custom Micromegas detector for TexAT was designed in collaboration with IRFU/DPhN Saclay (France) and fabricated at CERN using “bulk”- technology: the readout board, a photoresist layer ($128 \mu\text{m}$ thick) and the cloth mesh (stainless- steel wires of $18 \mu\text{m}$ diameter interwoven at a pitch of $63 \mu\text{m}$) were encapsulated together and then etched, producing the embedded $300 \mu\text{m}$ photoresist pillars in the mesh every $5000 \mu\text{m}$ in one single process [19].

The amplification (avalanche) gap of $128 \mu\text{m}$ between anode pads and embedded mesh allows for gas gains of up to the 10^4 - 10^5 . For the stable operation of detector in proportional mode the total charge of avalanche should be below the so-called Raether limit ([20]) before the gas discharge occurs. The Raether limit depends on detector geometry and gas composition. It was shown (see [21]) that the Raether limit for Micromegas detectors and majority of gases is at the level of 10^7 electrons. For TexAT detector the high gain is required to reliably detect protons, deuterons and tritons at side- areas (see Section 2.1.2) of TPC. The minimum possible energy losses of protons for typical experiments with TexAT are $\sim \text{keV/mm}$, producing few dozens of electron-ion pairs per mm on average. Thus, with typical gains of about 10^4 - 10^5 , a proton can create a total charge of avalanche at the level of 10^6 - 10^7 electrons, which is below (or close to) the Raether limit, but sufficient to observe proton tracks.

2.1.2. Micromegas Detector Readout Board Configuration

A rectangular ($346 \times 316 \text{ mm}^2$) Micromegas PCB has an active area of $224 \times 240 \text{ mm}^2$. To reduce the total number of channels a unique segmentation/multiplexing scheme was conceived, consisting of rectangular pads in the beam region and overlapping strips and chains to the left and right of the central region. The total number of Micromegas readout channels is 1,024. The board is divided into three areas as shown in Fig. 2: the zone to the left of a beam axis (L), the beam axis zone (C) and the zone to the right of the beam axis (R).

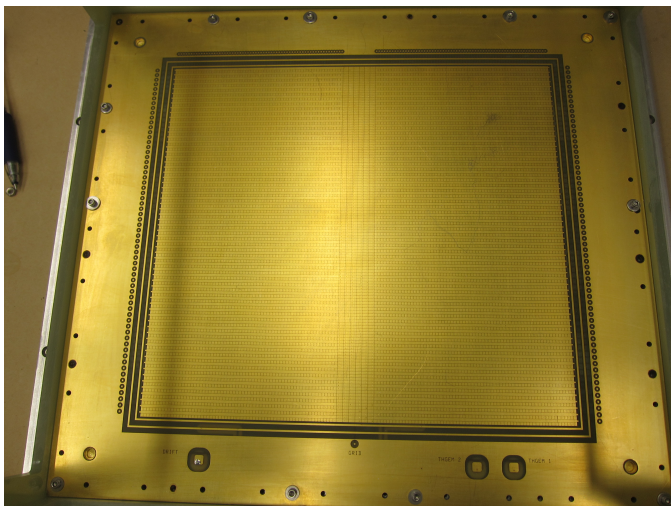
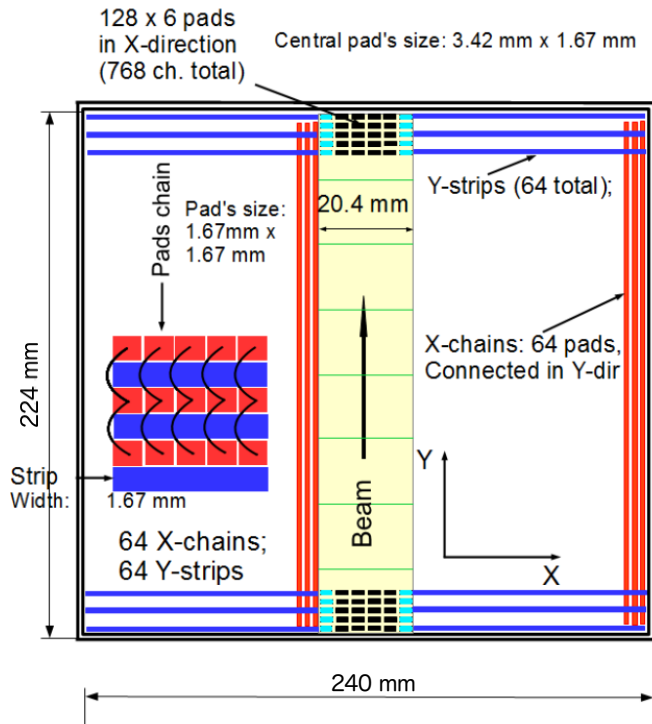


Figure 2: Top panel: The design of an active area of Micromegas PCB. The central region consists of 6 columns with the cyan pads on either side corresponding to side-pads. The strips in the side planes are the solid readout pads that are perpendicular to the beam axis while the chains are the square readout pads in the side regions that go along the beam axis. Bottom panel: Picture of the readout board.

The central zone (shown in yellow in Fig. 2, top panel) along the beam axis is 20.4 mm wide and has high segmentation: $128 \times 6 = 768$ individual pads (the pad size is $1.67 \times 3.42 \text{ mm}^2$). The pads are arranged so that there are 128 pads in the direction of the beam (along 224 mm side) and 6 pads in the direction perpendicular to the beam.

Both left (L) and right (R) zones are identical and have dimensions of $224 \times 101.5 \text{ mm}^2$. Each consists of 64 strips, perpendicular to the beam axis. The strip is $1.67 \times 101.5 \text{ mm}^2$. There is 1.75 mm of space between strips to allow for an individual pad to be placed between the strips. The distance between the centers of the strips is 3.5 mm. There are 64 individual $1.67 \times 1.67 \text{ mm}^2$ pads between each two strips. The pads located at the same distance from the beam axis are connected into chains, so that there are 64 “chains” of 64 interconnected pads arranged in the direction parallel to the beams axis in each of the side zones. Although the strips and chains individually cannot provide an accurate location for tracking (because each strip and chain run along either the beam axis or perpendicular to the beam axis) they can be matched together to make a 2D point (see Section 4.2). A picture of the TexAT Micromegas readout board without the mesh (the blank) is shown in the bottom panel of Fig. 2.

The signal readout of Micromegas board is carried out through the 80-pin (only 64 channels are active) high density (0.8 mm pitch) Edge Rate[®] Rugged High-Speed SAMTEC connectors. An optimized signal readout channel map has been designed. According to this map, the PCB has been segmented into different geometric zones of 64 channels:

- the central (“beam”) area (4 most central pads in each of 128 rows, 512 pads total) is divided to eight zones (shown by green lines in the top panel of Fig. 2).
- the left and right side pads of central area form two columns of 2×64 pads each (shown by cyan in the top panel of Fig. 2).
- zone (L) and (R) are parted in the following way: the group of 32 upstream strips and 32 far from the beam area chains combine into single readout zone; the 32 downstream (top at Fig. 2 strips and 32 close to the center chains make another one.

Following the form-factor of the readout electronics, described in Section 2.4, the zone’s readout is organized in a specified way: 2×256 channels from the most central area; 256 channels from the left zone (2×64 strips and chains) and left side columns of the central zone (2×64 pads), and 256 channels from the right zone (2×64 chips and chains) and right side columns of the central zone (2×64 pads).

Such segmentation facilitates the signal routing and allows to individually bias pads in the separate zones, giving a possibility to create avalanche areas with different gas gains within the single Micromegas detector. It will be shown below (see Sec. 5.3) how useful this feature is.

2.2. Field cage

Transparent for the beam ions and reaction products, the field cage maintains the uniform electric field inside a TPC volume with sufficient strength to provide a steady drift of electrons. The basic geometry of the cage surrounding the TPC is constrained by the Micromegas' readout board design and the solid state detector's wall design: 316 mm (L) x 346 mm (W) x 135mm (H). A 50 μm (diameter) gold plated tungsten wire has been chosen as the main element for the cage. The conversion drift volume is located between a transparent cathode, which is normally set to the high "negative" potential (-1000 \div - 3000 V) and a grounded mesh, transparent for electrons.

The electrons released in a process of gas ionization by charged products drift toward the mesh and amplified at the Micromegas in avalanches (the mechanism of gas ionization is described in detail, for example in [18].)

The homogeneous electric field is supported by the set of guide wires, stretched along the walls perimeter, stepped down from the negative potential of the cathode to the anode continuously by voltage division using a series of 25 M Ω resistors to create a uniform electric field. The resistors were hand-picked within a tolerance of 0.5 %.

A 3D- model of the TexAT field cage (shown in Figure 3) has been created using a finite element mesh generator GMSH[22]. To estimate the level of electric field uniformity and optimize wires spacing to create the best condition for electron drift inside the TPC, detailed simulations with computer codes GARFIELD [23] interfaced with Elmer [24] finite element analysis code have been performed.

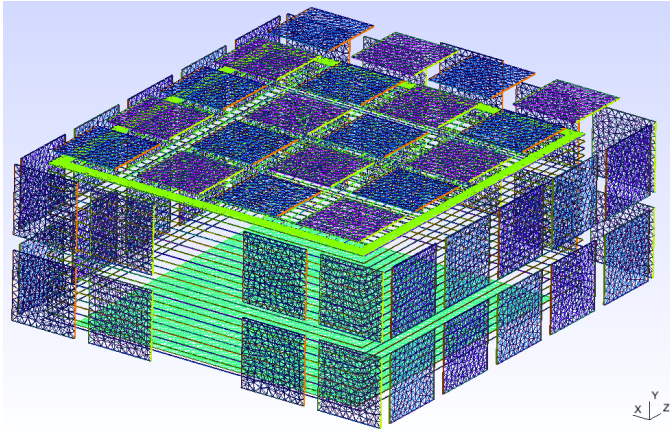


Figure 3: Simulated model of field cage for TexAT.

The Elmer Solver's Finite Element Analysis provides a map of the electric field at every point in the TPC. A simulated 3D-plot of the electrostatic field map inside TexAT TPC (the front of surrounding Si detectors is grounded) is shown in Figure 4. One can see that computed field appears to be relatively steady inside the active TPC volume while some deviations are manifested in the areas near boundaries of the cage and close to

Micromegas mesh. The aberrations of field uniformity are apparently induced by the leak of the electric field through the transparent cage and mesh.

The simulation of "realistic" configuration with the front side of Si detectors is under a full depletion potential of -200 V is shown in Figs. 5 and 6. A particular geometry of surrounding detectors enhances non-uniformity effect, especially at the "downstream"-side wall, that has a non-symmetric geometry (see Section 2.3 below).

The "edge" effects distort the electric force lines near the walls and create a dependence on the position of the track. These deviations can be reduced to some extent by increasing the guide wires density, but a compromise between a transparency factor, acceptable level of uniformity, and a practical fabrication has to be established. It has been determined, that the wire spacing of 5 mm provides a sufficient level of electric field uniformity inside the active volume of TPC. The 5 mm spacing allows for wire to be mounted on extension springs to avoid wire sagging, the technique developed for the ANASEN detector [6].

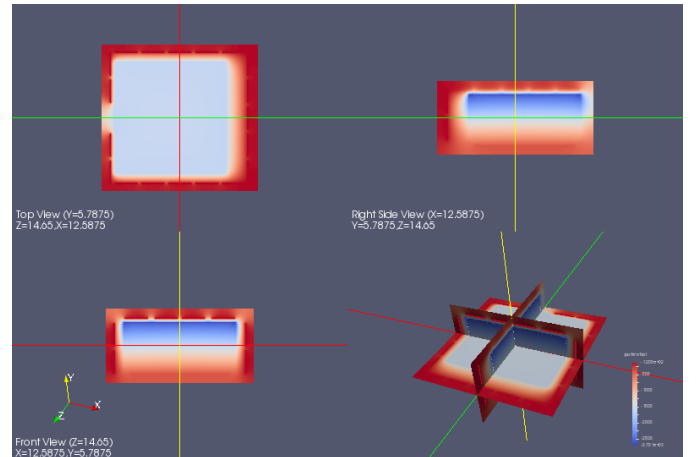


Figure 4: Electric field simulation.

The leak of positive potential on the pads through the transparent grounded mesh leads to the perceptible distortion of electric field (at the level of 10 \div 15%) near the mesh, which separates the "drift" volume from the "avalanche" region. This effect is unavoidable because of particular geometry, but further computation of electron transport in different gases (methane, butane, Ar/CO₂, He/CO₂ mixtures) using MAGBOLTZ [25] have defined the optimal conditions for constant electron drift velocity even in the presence of electric field aberrations. One example of such simulations is shown in Fig. 7 for Methane gas at different pressure. The "navy blue"- colored (shown online) area at the plot represents the optimal conditions for electron drift.

Another factor, that may deform an electric field is an "axial" geometry of the guide wires, instead of a classic "plane" guides. A horizontal electric field between the field cage and the walls leaks in the drift region, deforming the electron drift trajectory.

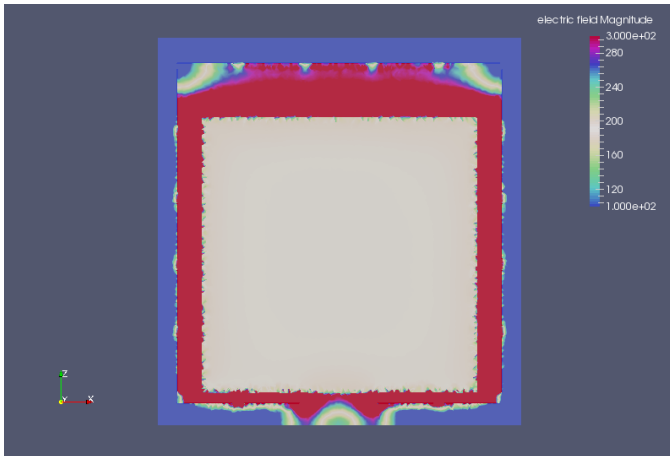


Figure 5: Electric field simulation: Top (XZ plane) view.

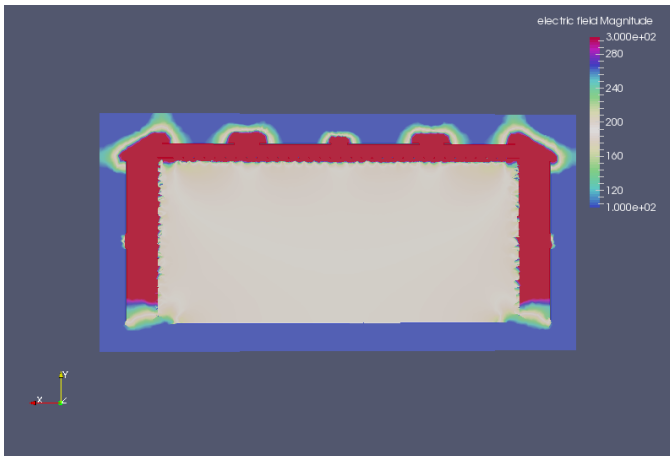


Figure 6: Electric field simulation: Side (XY plane) view.

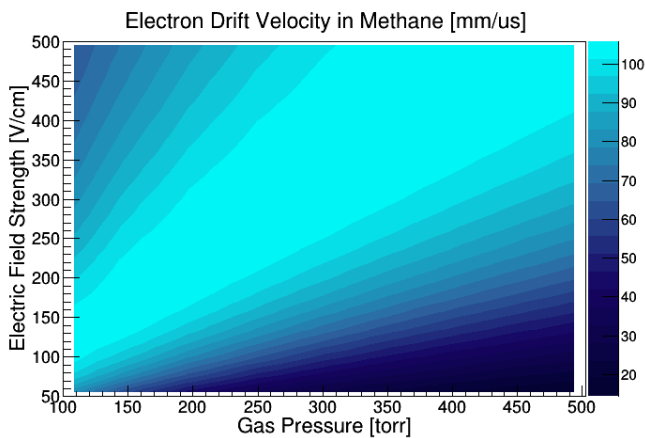


Figure 7: Electron drift time for different gas pressure and field strength.

To improve linearity near the edges the second set of wires was

introduced at a horizontal distance of 5 mm from the first set, as shown in Fig. 8. This second layer establishes the flat isopotential “plain”, reducing effects of electric field distortions near the edges.

The two wire cage with 5 mm vertical spacing and 5 mm horizontal distance between the two wires satisfied the condition of minimum non-uniformity of the electric field, 98% transparency and practical fabrication considerations. An example of a 2D track of a 5.5 MeV α -particle from ^{241}Am source in He+6%CO₂ mixture at the pressure of 50 Torr is shown in Fig. 9. In the bottom panel of Fig. 9 the X-axis is the distance from the entrance of the active area in mm and the Y-axis is the TPC electron drift time. The top panel is the projection of the track to the plane parallel to the Micromegas detector. No noticeable deviations from linearity are observed in either projection.

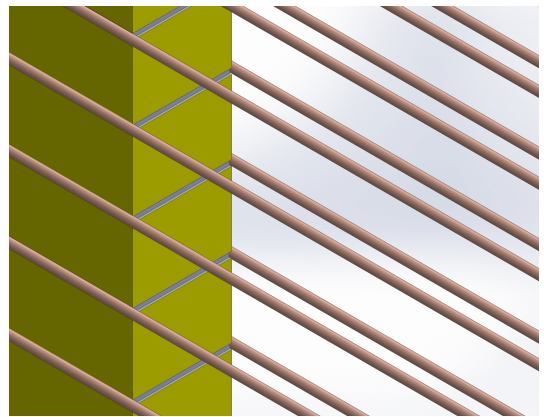


Figure 8: Rendering representation of double layer grid of TexAT field cage. The grey lines on the field cage frame are shown to indicate the double-wire “plain”.

2.3. Solid state detector array

Arrays of solid state detectors (Si and CsI) are used in TexAT to measure the total energy of particles that have escaped the active target volume and to provide an additional PID. Due to 3D tracking in the TPC, high segmentation for the Si wall is not necessary. Double side silicon detectors with an active area of 50×50 mm² were chosen to build a Si detector walls, surrounding the TPC. The principal requirements were high energy resolution, reliability and price to quality measure.

Three different types of Si detectors were used:

- MSQ25-1000 from Micron Semiconductor ([26]). The geometry is: four quadrant sectors (25×25 mm²) at junction side and single quadrant (50×50 mm²) at ohmic side. The typical energy resolution for α particles from the ^{241}Am source is 50 - 70 keV, and the total leakage current at full depletion is less than 1 μA (degraded to 3 μA after several in-beam experiments);
- W1-500 detector from Micron Semiconductor ([26]). This detector is often used downstream at the beam axis. It has 16 vertical junction strips at the front and 16 horizontal ohmic strips at the back. The width of the strips is 3 mm.

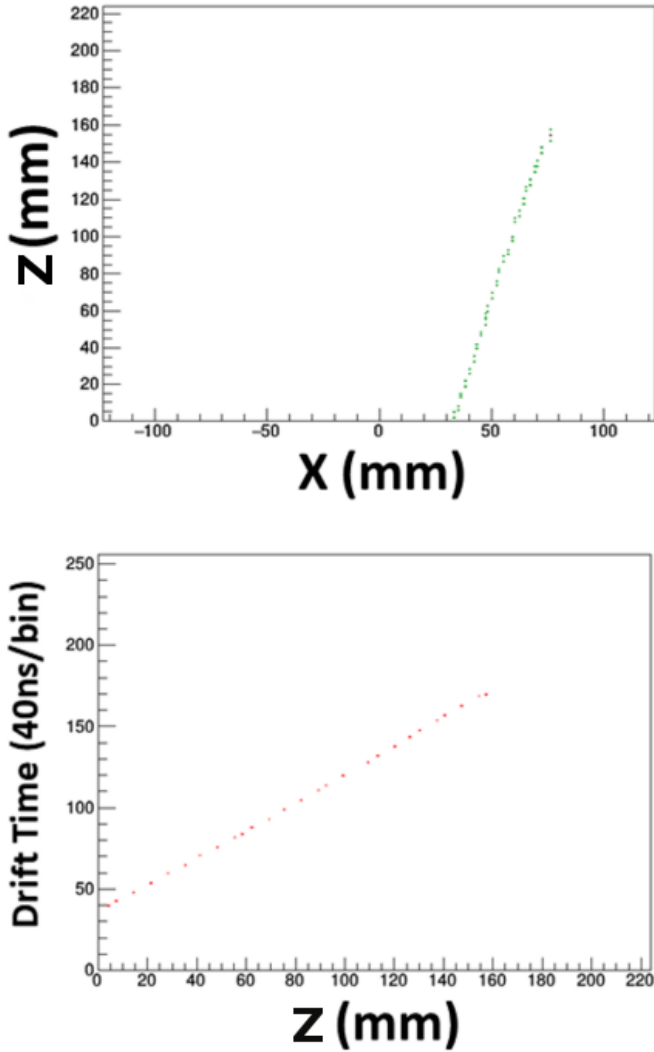


Figure 9: 2D track of an α -particle from ^{241}Am source in He+6%CO₂ mixture. Top panel: X-axis is the position perpendicular to the beam axis and Y-axis is the position parallel to the beam axis. Bottom panel: X-axis is the position of beam axis and Y-axis is electron drift time. The collimated α -source was placed at the upstream of the field cage along the beam axis outside of the Micromegas active area

Such geometry provides a position sensitivity of $3 \times 3 \text{ mm}^2$ allowing a service diagnostic during the secondary beam development and additional position sensitivity at small scattering angles for some experiments at low energy when the beam stops in the gas target.

- A test set of 12 total silicon four-segment charged particle detectors KDP-1K have been developed at the JSC “Institute in Physical-Technical Problems”, Dubna, Russia ([27]) for TexAT. The detectors were made of n-type Si (660 μm thick) using the ion implantation technology with thermal surface passivation. The input aperture of the detector is $54.1 \times 54.1 \text{ mm}^2$. The active area of each segment is $25.0 \times 25.0 \text{ mm}^2$ with a 50 micron gap between the segments. A system of common guard rings was used in the design of the detecting structures. The thickness of the

detectors of the delivered batch was 625 micron. Detectors were tested both with α -source and in-beam. Typical leakage currents of the segment at a full depletion bias voltage of 130 V were found to be less than 20 - 30 nA. The spectrometric characteristics of each quadrant of the detectors were measured with an α -source at the over-depletion bias voltage of 150 V. Typical values of the energy resolution were at the level of 30 - 40 keV FWHM under irradiation from the pn junction side. These detectors were in active use for 5 in-beam experiments and only one of 12 has lost the resolution below an acceptable level (75 keV). The properties of KDP-1K detectors are in compliance with technical requirements and it has been decided to make them a basic component for TexAT.

The supporting frames are slightly different but in principle MSQ25-1000 and KDP-1K are interchangeable with some small adjustment.

The outer layer of TexAT was composed from the thick CsI(Tl) scintillator detectors located at the back of all of the Si detectors. They can be used for detection of both charged particles and gamma rays. Cuboid-shaped 40 mm thick CsI(Tl) crystals have been selected to ensure that the full energy is measured for particles that can penetrate through the silicon detector. The geometry of crystals was chosen to match the Si detectors face: $50 \times 50 \text{ mm}^2$. Each crystal is wrapped in $2 \mu\text{m}$ thick aluminized mylar and has a built-on preamp which is read out by a single Hamamatsu $20 \times 20 \text{ cm}^2$ S3204 PIN diode. The role of the CsI(Tl) array in the TexAT chamber is primarily to identify and measure residual energy of particles that punch-through the Si detectors. Using an ^{241}Am α -source, we have determined the energy resolution for the CsI(Tl) detectors to be about 5%.

Solid state telescopes are arranged in 4 different configurations matching the TPC geometry (shown in Fig. 10). All side’s arrays are mounted at independent doors providing an easy access to the scattering chamber and handy replacement of components. The bottom array is placed onto the main body of the TexAT scattering chamber.

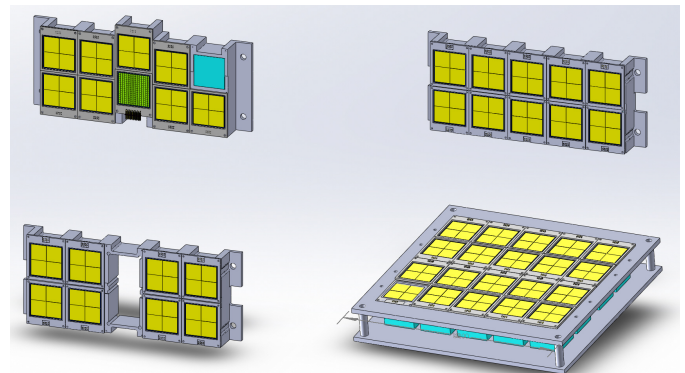


Figure 10: Rendering of the solid state telescopes of TexAT array: Forward array (top left); Side array (top right); Backward array (bottom left); Bottom array (bottom right). One of forward Si detector is removed to show an arrangement of CsI(Tl) scintillation detectors.

Auxiliary detector systems, such as a windowless ionization

chamber located at the entrance of the TexAT scattering chamber, right after the entrance window, and a scintillator located before the entrance window in vacuum have been used for some (but not all) TexAT experiments for normalization and beam diagnostics. These systems are not part of TexAT and will not be discussed further in this paper.

2.4. Readout electronics

The electronics channel count for TexAT is 1,024 channels for TPC readout, 232 channels for Si detectors and 58 channels for CsI(Tl) scintillation detectors, for a total of 1,314 channels. The readout electronics for all of these detectors is based on General Electronics for TPCs (GET). The details of the GET system are published in Ref. [28]. Briefly, the TexAT readout system consists of 24 AGET chips. The AGET chip amplifies and shapes the signals while performing pole-zero corrections. For each channel, the signal is stored in 512 time buckets (using switch capacitor arrays) with a frequency that can vary between 1 to 100 MHz (from $1\mu\text{s}$ to 10 ns per time bucket). The signals are compared to a threshold to provide a channel-level trigger. Each AGET chip has 64 independent channels and includes four extra channels to measure the noise. These “noise” channels are structurally identical to the 64 input channels and provide a way to subtract the electronic noise in the system.

The 24 AGET chips are installed onto 6 AsAd boards (4 chips per boards). The main role of the AsAd board is to digitize the signals from each AGET chip when a trigger is issued. The digitizer of the AsAd board is a four channel 12-bit ADC [28]. Up to four AsAd boards can be connected to the top level of the GET electronics, the CoBo (**C**oncentration **B**oard). When a trigger is sent to the CoBo, it collects and time stamps the data and sends the data to be stored. An additional board called the MuTAnT (**M**ultiplicity **T**rigger **A**nd **T**ime) is used to synchronize all of the CoBos. The MuTAnT board also collects the triggers from all of the CoBos and generates a global trigger. There are three different types of triggers in the GET system: Level 0, Level 1 and Level 2. The Level 0 trigger is an external trigger. A Level 1 trigger is obtained by summing the multiplicity triggers from the CoBos to generate a global trigger. The last trigger type, Level 2, can trigger on complex predefined pattern of channels that fired. The Level 2 trigger has not been tested with TexAT yet.

2.5. Transition ZAP- boards

To connect detectors to the AsAd cards, a special readout adapter board (referred as ZAP) has been designed for each kind of detector (MM, Si and CsI(Tl)). The ZAP-board allows the readout of signals from the detectors, to bias them (individually or in groups) and to protect the sensitive electronics of the AsAd cards and AGET chips from the electrical breakdown caused by potential sparks in Micromegas detector.

The PCB design was made using prototyping software Design Spark PCB 7.1 [29]. The boards have 4 layers and all elements are surface mounted. The electronic components are placed outside of TexAT scattering chamber to simplify the replacement in case of electronic failures. All transition ZAP-

boards have a similar form-factor. They are epoxy-sealed to the custom vacuum flange, making a signal feed-through to the TexAT scattering chamber.

2.5.1. Micromegas ZAP- board design

The basic circuitry for the signal readout allowing protection, suggested by developers of GET electronics ([30]). The protection circuitry is based on a diode bridge. A “common mesh” circuit is used for TexAT’s Micromegas detector: pads/strips/chains were set at positive DC potential (200 to 600 V) to create an avalanche in Micromegas detector. Such an approach allows the tension to be set individually at different zones of the TexAT Micromegas detector (see Sec. 5.3) to create avalanche areas with different gas gain. The board-to-board connection concept was used to reduce noise and to avoid eventual connection problems with high density cables between electronic components. Every Micromegas ZAP card has 4 individual biasing lines through the SHV- connectors to ensure smooth functioning at the higher tension ($> 400\text{ V}$). Micromegas ZAP “input” interface matches to MM readout board interface (SAMTEC male/female) and the “output” ZAP- interface matches to AsAD card interface (SAMTEC female/male).

The micromesh is either grounded or fed to the charge sensitive preamplifier (Canberra). In the latter case, the signal from the mesh can be monitored with an oscilloscope and/or to be used to generate a trigger.

2.5.2. Si detectors ZAP-board design

A ZAP card consists of four identical groups of channels, each one maintains up to 16×4 quadrant Si detectors (MSQ25-1000 or KDP-1K, 64 total individual channels). The Si detectors connected to ZAP board inside scattering chamber by flat cables combining 8 detector outputs to 32 ribbon cable, plugged to standard 34 pin header. $10\text{M}\Omega$ resistors is used instead of ($10\text{M}\Omega - 100\text{M}\Omega$). Detectors are biased through the 16 position connector header with a single bias line supporting 4 Si detector front channels. In the full configuration, TexAT consists of 58 Si detectors. The current ZAP-board configuration allows to read out signals from the “front”- side of all detectors provided that “backs” of all detectors are common. The signals from the back side of Si detectors can be also readout, but in this case the total number of detectors is limited to 48 (a single AGET is not able to work with “mixed” polarity signals). All Si detectors are biased from MPOD Power supply unit.

Signals from the detectors go through the SAMTEC connectors to the internal AGET preamplifier.

2.5.3. CsI(Tl) scintillation detectors ZAP- board design

Signals from the CsI(Tl) scintillation detector were output of its own custom preamplifier, located right on the PIN diode to reduce the electronic noise. The Charge Sensitive pre-Amplifier (CSA) function and filter stages of the AGET chip are bypassed. In addition, the “slow” output of the detector required an optimal peaking time of 4 to 6 μs , while the available range of peaking time for the AGET chip extends from 50 ns to 1 μs (sixteen values total). In order to optimize the signal processing of

the detector, we use a 16-channel MESYTEC shaper (MSCF-16) [31] and feed the shaped output signals into an Inverting x2 Gain (G-2) function of the AGET chips (See [30] for details). The G-2 stage provides an extra inverting voltage gain and a buffering for signal sampling in a Switch Capacitor Array (SCA) in the AGET chip. The offset voltage of the Gain-2 input signal was adjusted by the non-inverting level shifter circuit with the 75 MHz gain bandwidth LM6154BCM Operational Amplifier (OpAmp) [32] (Fig. 11), depending on the polarity of input signals: +2.2 V for positive polarity or 0.7 V for negative polarity.

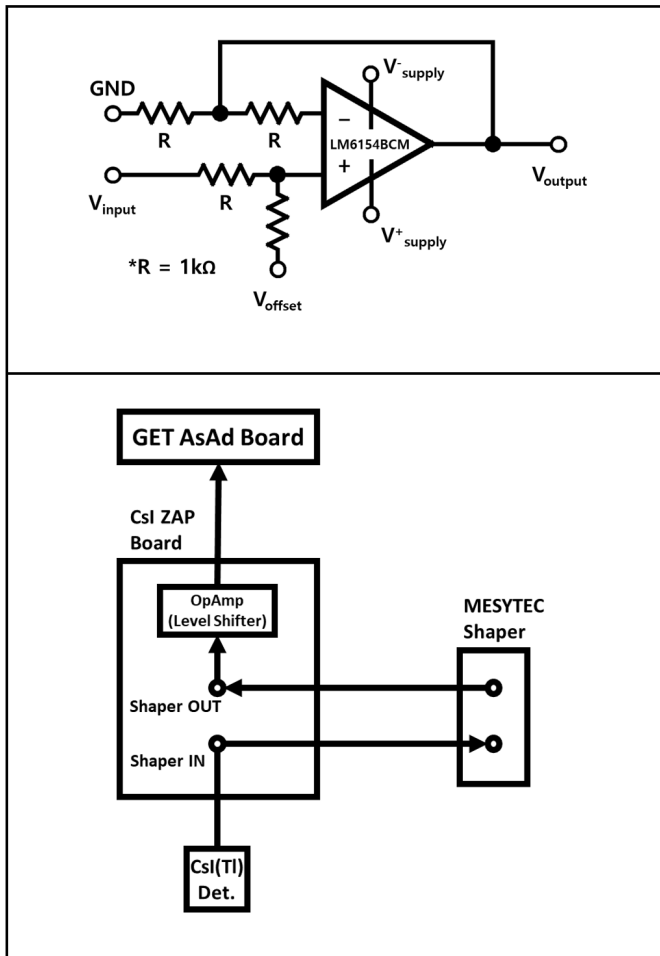


Figure 11: Top: A schematic of the non-inverting level shifter circuit using the LM6154BCM OpAmp. The supply voltage, V_{supply} or V_{supply}^- , was adjusted to match the impedance of the circuit and GET electronics input. Bottom: A signal processing diagram using the external shaper for CsI(Tl) scintillation detector.

A custom ZAP board has also been designed. The sixteen total fast OpAmp integration circuits were implemented on the board. While one offset voltage and one supply input can be set for all the OpAmp circuits, one OpAmp handles 4 independent channels resulting in 16 outputs for each AGET chip input corresponding to the full channel numbers of one MESYTEC module. One ZAP board allows us to process signals from 64 total CsI detectors, placed inside the TexAT chamber.

2.6. Scattering Chamber

A custom scattering chamber has been designed to hold the detector array and to maintain the workable conditions for both gaseous (Micromegas and ion chamber) and solid state (silicon and scintillation) detectors. It has an aluminum body/shell of cuboid shape: 508mm x 508mm x 343mm, made from 25.4 mm thick aluminum sheet. The top cover is designed to secure a Micromegas based time-projection chamber (TPC). It also has six slots for vacuum feedthroughs (ZAP-boards) to read out the anode signals from Micromegas and solid state (semiconductor and scintillation) detectors. The general layout of scattering chamber parts is shown in Fig. 12. All readout electronics are coupled directly to the feedthroughs, eliminating cables. (Fig. 12

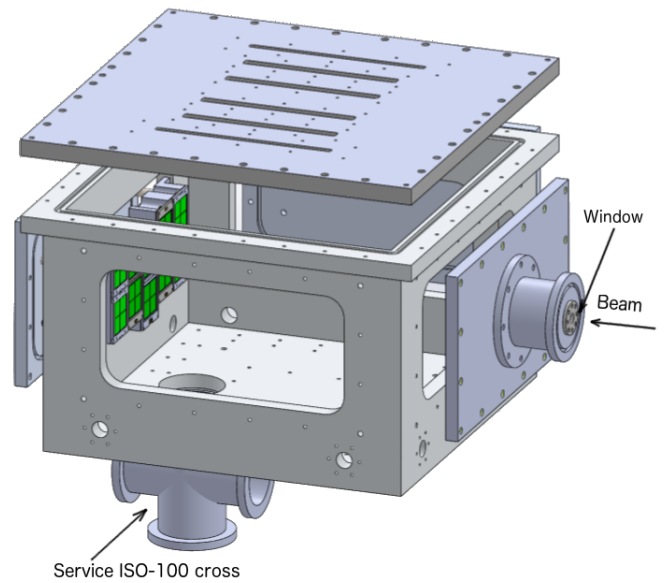


Figure 12: 3D- drawing of TexAT scattering chamber. One of the Si/CsI(Tl) detector array is shown attached to the "forward"- door

Each of the four chamber's sides has a square 355.6 mm by 203.2 mm) port, plugged with a O-ring's vacuum sealed doors. Such design allows one to mount solid state detectors, surrounding the TPC at each flange independently. It provides an easy access to all components of detector array and versatile installation at any beam line (either at in-flight exotic secondary beam line using MARS- separator, or at future project of re-accelerated exotic beam line) through the standard ISO-100 upstream vacuum flange. The scattering chamber's gas volume is separated from the beam line with a thin vacuum tied Havar/Kapton/Mylar entrance window with a diameter of 12.5 mm, mounted at the forward wall, connecting TexAT to the beam-pipe (shown in (Fig. 12).

A small planar windowless Ion Chamber (IC) with a Frisch grid can be mounted at upstream flange. The IC works in the same target gas media to provide a particle ID and count ions of incoming beam and also provides additional normalization and beam-tracking capabilities.

The bottom side of the chamber is equipped with ISO-100

compatible style port for vacuum pumps connection. Another set of KF40 ports are placed on the side walls (2 at each wall, 8 total). These ports are used for gas inlet/outlet, vacuum/pressure/temperature sensors, IC voltage/readout and high voltage feedthroughs, supplying different circuits.

The chamber finish is mechanically polished and de-ionized to meet the pretty narrow requirement for steady operation of the Micromegas detector which is sensitive to impurities and dust. The tested chamber leak rate was in the range of 10^{-8} atm-cc/sec. All major operations with TexAT (e.g., mounting of MM-, Si- and scintillation- detectors, etc.) during the experiment's preparation are conducted in a clean room environment.

2.7. Gas handling system

The multipurpose vacuum and gas handling system has been developed to provide a possibility of running experiments with exotic beams in both “detector” (for example, decay-experiments) and “active target” (resonance scattering, transfer reactions, etc.) modes. It is similar to those built for the ANASEN detector [6]. The gas pressure and flow is controlled by an integrated pressure controller with mass flow meter π PC-99 from MKS Instruments. It can control gas pressure through TCP/IP protocol at the range of 15 Torr to 1250 Torr with an accuracy of $\pm 1\%$. The system was tested for gases like helium/ CO_2 mixture, carbon dioxide, argon and mixtures (P5/P10). It also meets safety specifications for use of flammable gases (hydrogen/deuterium, methane, iso-butane, etc.) and was tested with those gases as well.

The reliability of the system has been demonstrated during several 3 - 4 week long runs.

3. TexAT Monte Carlo Simulation Package

A complete TexAT Monte Carlo simulation package was developed utilizing the Geant4 [33] and Garfield++ [23] libraries. Two reactions were studied as the test cases: $^{12}\text{C}(p,p)^{12}\text{C}$ and $^{18}\text{Ne}(\alpha,p)^{21}\text{Na}$. In the latter, residual ^{21}Na nuclei in both the ground state and first excited state were populated. In the simulation, the incoming ions were forced to undergo the reaction of interest at a random point within the TPC using binary reaction kinematics. At each step of an incoming or product track, the total ionization energy was converted to a number of electron and ion pairs, and each electron was drifted under a constant electric field to the Micromegas board. Time-dependent histograms of the number of detected electrons for each pad of the Micromegas board were generated and stored for offline processing incorporating the properties of the gas being simulated. Additionally, the energy collected in each detector of the silicon array was also recorded per event. Fig. 13 shows an example event visualized in Geant4.

Custom track reconstruction routines have been developed for the TexAT detector. For particles traversing the left and right regions, X-Y coordinates are determined by matching strips to chains (or vice versa) using the average recorded drift time. In the central region, the X-Y coordinates of a track are determined solely from the position of the rectangular pad with the

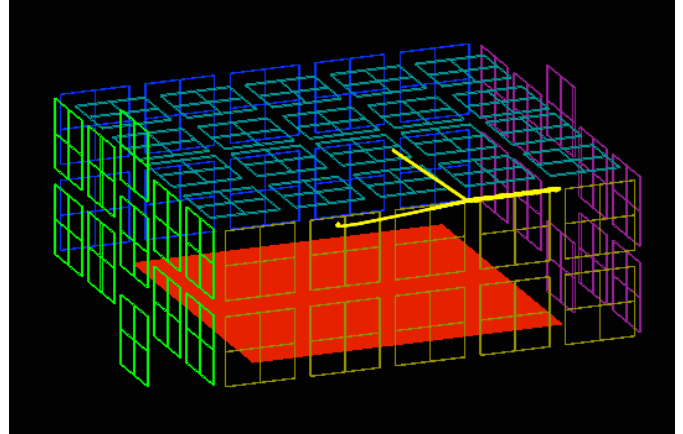


Figure 13: Example of simulated track for the $^4\text{He}(^{18}\text{Ne},p)^{21}\text{Na}$ reaction in the TexAT detector as visualized in Geant4. The light recoil (proton) hits the Si detector on the top plate and the heavy recoil (^{21}Na) stops in the gas volume.

highest energy deposition per row. Such a procedure yields two tracks: one for the light product and one combined track for the incoming ion and heavy recoil. By finding the point of closest approach of the fitted light product and the heavy ion tracks, the heavy ion track in the central region can be split into separate incoming and recoil tracks. Finally, the three tracks are re-fit simultaneously to find the vertex of the interaction and the relative angles of the reaction products extracted. Fig. 13 shows an example of this track reconstruction.

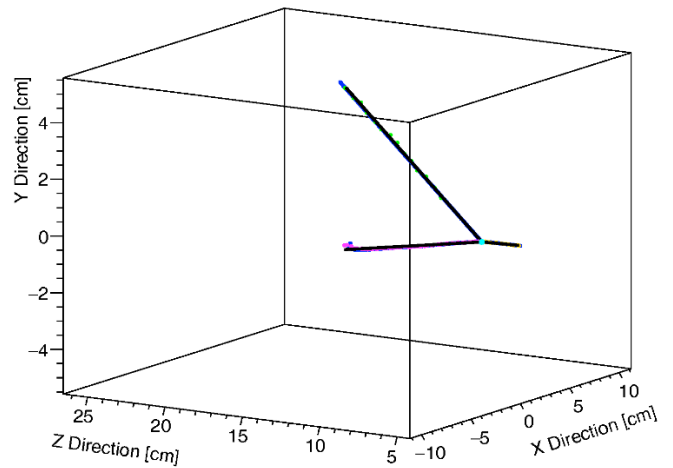


Figure 14: Same track as in Fig. 13, but reconstructed from drifted electrons detected by the Micromegas pads.

The blue points are the simulated interaction points, while the yellow, purple and green points are reconstructed from the information recorded from the simulation for the Micromegas board. The black lines are the fitted tracks, and the cyan point indicates the fitted reaction vertex. For the reactions of interest, the vertex reconstruction error was found to be approximately 1.5 mm on average, with a distribution that peaked below 1 mm. The angular resolution determined from the simulation was ap-

proximately 3° at FWHM. If the Q-value of the reaction is unknown, the center of mass energy of the interaction can only be reconstructed from the vertex position and the average energy loss in the gas, and is limited by energy straggling effects. For the incoming ^{18}Ne ions, this yielded a center of mass energy resolution of 190 keV at FWHM. Using the interaction energy as provided by the vertex, in addition to the angle and energy (measured in Si detectors) of the light product, the Q-value can be reconstructed. In the case of the $^{18}\text{Ne}(\alpha,p)^{21}\text{Na}$ reaction, transitions to the ground and first excited states of ^{21}Na (separated by only 330 keV) could be well resolved (see Fig. 15). (Assuming that energy resolution of the incoming ^{18}Ne beam corresponds to the “typical” energy resolution of reaccelerated radioactive beams.)

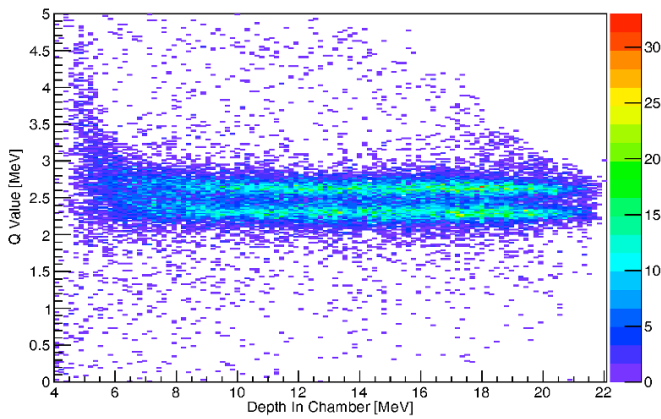


Figure 15: Reconstructed Q-value vs. chamber depth as determined by the energy of the ^{18}Ne for the simulated $^{18}\text{Ne}(\alpha,p)^{21}\text{Na}$ reaction

Once the reaction mechanism is identified (e.g. elastic or inelastic scattering), the center of mass energy resolution can be improved by recalculating using the Q-value, the detected energy in the Si detector, and emitted light product angle. In the present study, the center of mass energy resolution for these events was found to be 40 keV at FWHM (see Fig. 16).

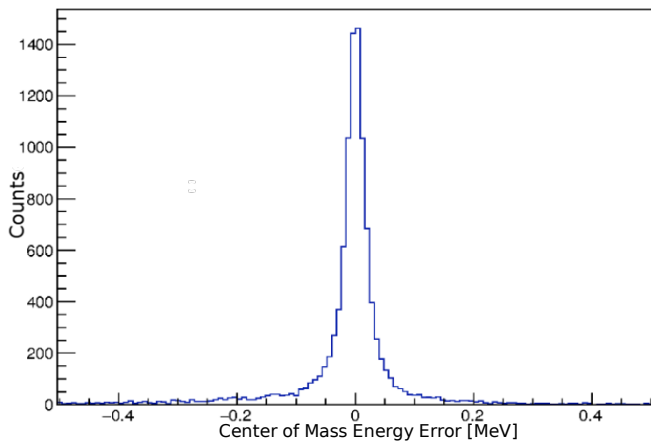


Figure 16: Center of mass energy resolution for the simulated $^{12}\text{C}(p,p)^{12}\text{C}$ reaction.

Additionally, these energy and angle resolutions were found to be mostly insensitive to the depth within the scattering chamber and therefore interaction energy and scattering angle. The simulations demonstrate that the segmentation implemented in TexAT is sufficient to reconstruct the observables with high enough precision to identify the events due to population of two closely spaced excited states (~ 300 keV) in the (α,p) reaction. It was shown that track reconstruction allows for energy resolution of 40 keV and angular resolution of $\sim 3^\circ$ over wide range of excitation energies and scattering angles.

4. Data Analysis

The analysis of the data recorded using the GET DAQ with the TexAT detector involves a multi-step process. It involves subtraction of the baseline for all signals, the wave form fitting to determine waveform maximum amplitude values and peak times, matching chains and strips in the side region to create three-dimensional points for track reconstruction and fitting tracks using various methods for noise reduction.

4.1. Baseline Corrections and Obtaining the Energy and Timing

The AGET chips have 64 input channels but provide 68 output channels. Four of these channels are called fixed-pattern noise (FPN) channels that are not connected to any detector and record the intrinsic noise and electronic baseline [28]. These four channels are averaged together and subtracted from each waveform of the remaining 64 channels to remove the intrinsic noise in the electronics. Examples of the FPN channels and raw waveforms are shown in Figure 17.

Further correction is achieved by subtracting the overall baseline, found by averaging the first and last 10 time buckets, from the FPN corrected signal. Examples of the waveforms corrected by the FPN and baseline subtraction are shown in Fig. 18.

4.2. Chain and Strip Matching

To perform track reconstruction in the side regions of the Micromegas detector, chains and strips must be converted to matched X-Y pixels since they only contain either X-pixel of the track (strips) or Y-pixel of the track (chains), respectively, as shown in the top panel of Fig. 2. This matching process can be done by using the time of the signal recorded for each channel. When the charged particle travels over the side region, any X-pixel from strips and Y-pixel from chains that correspond to the proton track position should have the same drift time. If the track is not parallel to the Micromegas plane (time among strips or chains > 40 ns), the matched X-Y pixels based on the same signal time within 40 ns should form a well defined track. An example of such event is shown in Figure 19. When the track is parallel to the Micromegas detector (time among strips or chains < 40 ns), the timing for the chains and strips will be the same and the matched X-Y pixels form a square instead of a defined track like that in Figure 19. For cases like this, the first point in the matched square closest to the origin and the point furthest away from the origin are chosen to form the track.

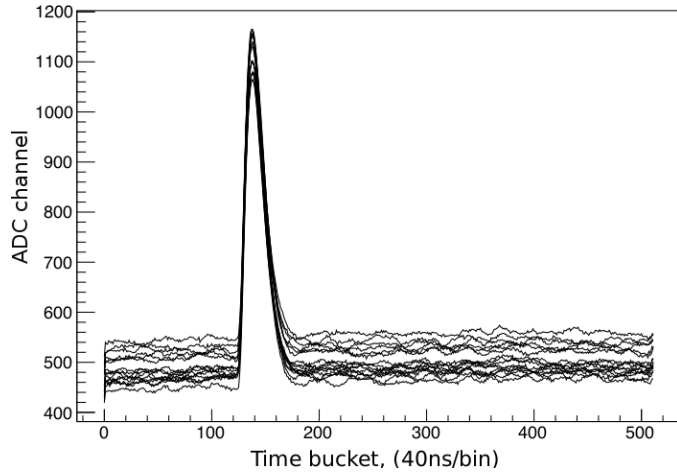
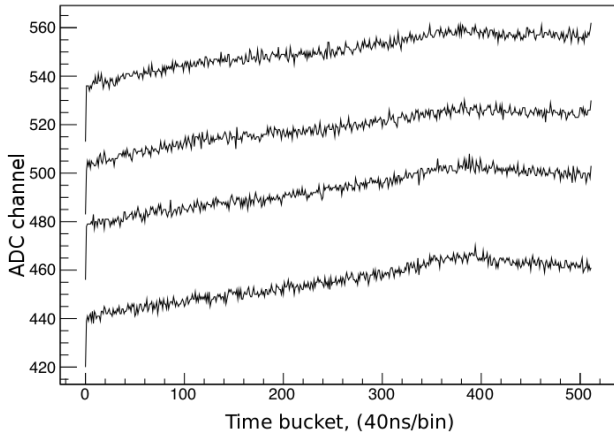


Figure 17: (Top) Example waveforms of the four FPN channels. (Bottom) Raw Waveforms without any FPN or background subtraction.

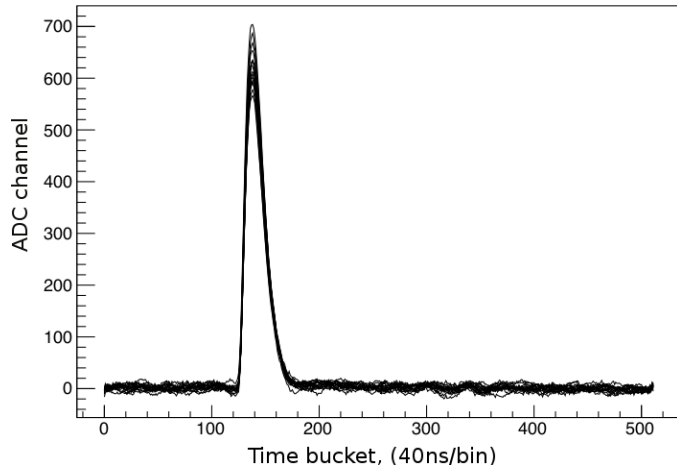


Figure 18: Waveforms corrected with FPN and background subtraction.

4.3. Track Reconstruction - Hough Transform

The signal in the TPC is often contaminated by “noise” - random pads firing in coincidence with the track but seemingly unrelated to it. We have used the two dimensional Hough transform to reduce the influence of this “noise” on the track reconstruction.

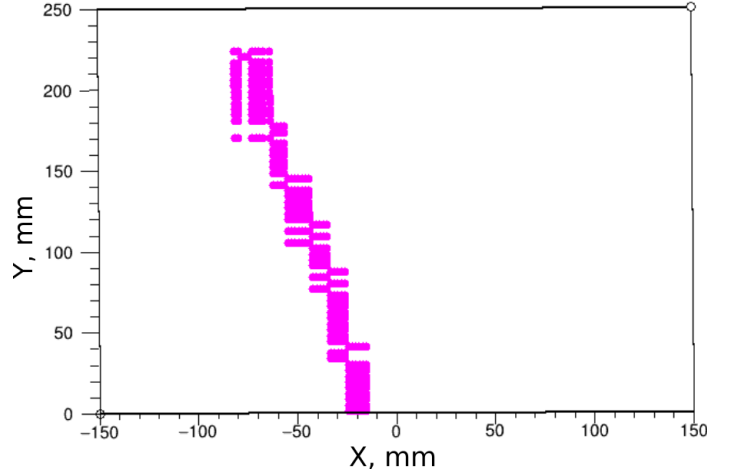


Figure 19: An example of matched chains and strips for a single event that can then be used to reconstruct a track.

The Hough transform is a feature extraction technique that has been very successful in image analysis and image processing [34]. The Hough transform was originally used to identify lines in an image and in this analysis, to find tracks (lines) through data points. This method works by transforming points into a parameter space and a voting procedure is used to find peaks in this parameter space. For each point (x, y) the Hesse normal form is calculated.

$$d = x \cos \theta + y \sin \theta, \quad (1)$$

where d is the distance of closest approach to the origin and θ is the angle between the x-axis and the line connecting the origin to the closest point as shown in Figure 20. The (d, θ) parameter space is called the Hough space. For every point in the data, θ is varied from 0 to π and d is calculated.

The algorithm used to find the optimal (d, θ) was to search through all angles and find the lowest standard deviation in d . A simple example with noise is shown in Figure 21. In the top of Figure 21, there is a straight line formed by the blue colored points while the orange colored points are noise. The Hough space is shown at the bottom of Figure 21 illustrating the point where the standard deviation is minimal. By finding the optimal parameters (d, θ) , we find the best fit of the data that is not affected by noise.

4.4. Alpha Source Test in Gas

The chains and strips matching technique and a technique to fit tracks with noise using the Hough transform using an α source in gas were tested. The gas chosen for this measurement was methane at 50 Torr so that the 5 MeV α particles propagate through the entire active volume of the scattering chamber and make it to the Si detector while also depositing enough energy in the gas to make tracks. The α source was placed approximately 60 mm behind the Micromegas plate facing the Si detectors. An accumulation of the tracks in the XY-plane are shown in Fig. 22. Zero on the y-axis in Figure 22 corresponds to the start of the Micromegas plate and shown are all the tracks

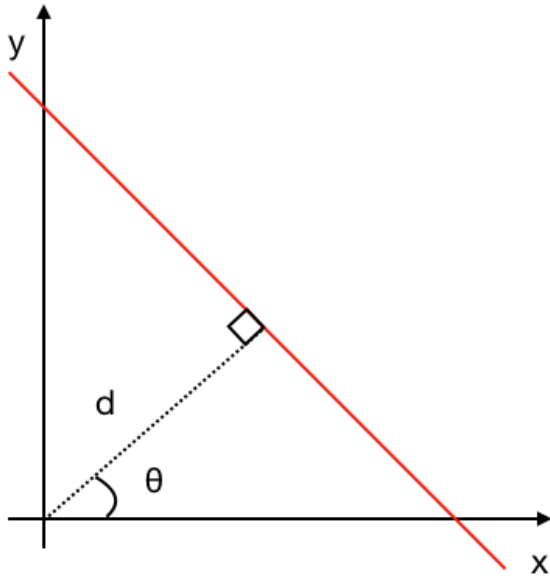


Figure 20: Diagram of the d, θ parameters in two dimensions.

that end up in the forward and side wall Si detectors. The tracks are converging at the $(0 \text{ mm}, -60 \text{ mm})$ point that has about the size of the source ($\sim 5 \text{ mm}$ along the x -axis).

Beyond plotting the XY-plane of all the tracks, we also judge how well our track reconstruction performs by plotting the projected end point of the track at the location of the Si detectors plane. When fitting the tracks, none of the Si information is used to constrain the track reconstruction. The XZ-plan reconstruction of track end point at the location of the Si detectors for the forward wall are shown in Figure 23. We clearly see the definitions of all nine Si detectors on the forward wall and also the gap corresponding to the missing Si detector in the top left corner. Although no Si information is used in the track reconstruction, it is recorded which Si quadrant fired. By using this information, we can get a better idea to how well the track reconstruction is by only plotting the XZ projection if certain quadrants have fired. By plotting the reconstructed track end-points only for opposite corners of the Si detectors a checker-board pattern is achieved, just as expected 24. Very good position reconstruction for each of the quadrants is evident.

5. Commissioning experiments

To date we have conducted four types of experiments with TexAT:

- Resonance elastic scattering of protons with stable and rare isotope beams - $^{12}\text{C}+p$ and $^8\text{B}+p$
- Resonance elastic scattering of α -particles with rare isotope beams - $^{10}\text{C}+\alpha$ and $^{14}\text{O}+\alpha$
- Direct measurements of fusion reaction cross section - $^8\text{B}+^{40}\text{Ar}$

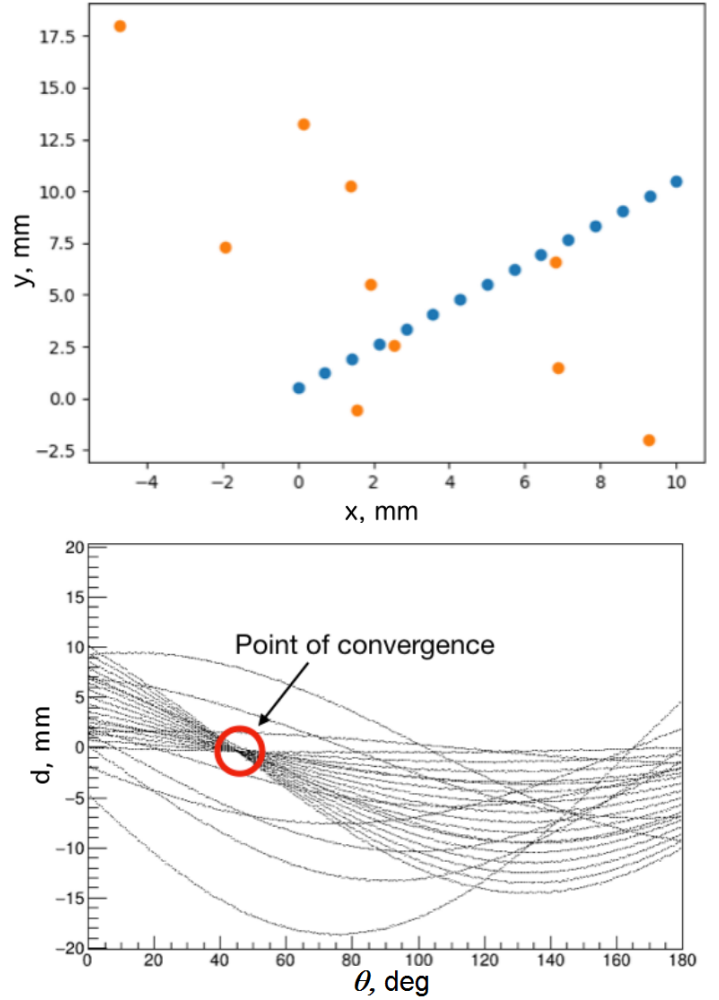


Figure 21: (Top) A straight line (blue points) with scattering noise (orange). (Bottom) The Hough space of the top points. Outlined in the red is the minimal standard deviation of d corresponding to the straight line of blue points.

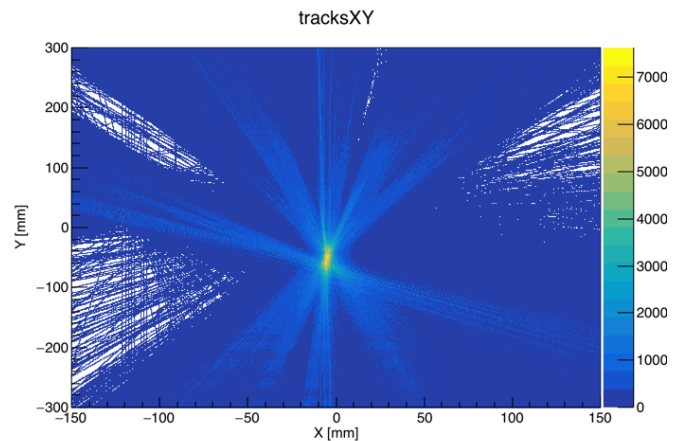


Figure 22: An accumulation of the alpha source tracks in the XY-plan in the forward and side walls. 0 mm on y -axis corresponds to the beginning of the Micromegas plate. All of the tracks converge to $\sim -60 \text{ mm}$ where the source was located.

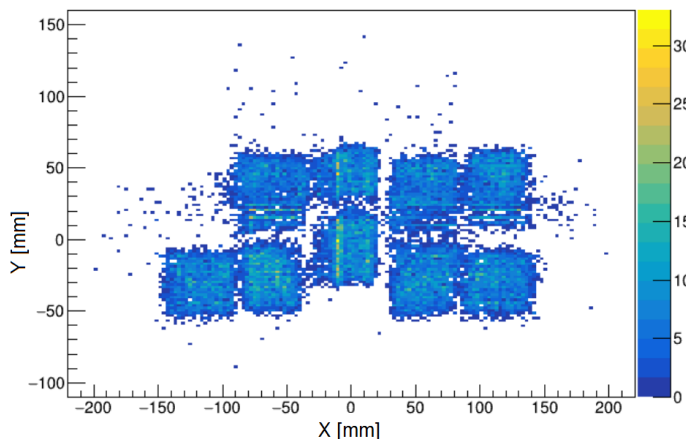


Figure 23: The XZ projection of the forward Si wall.

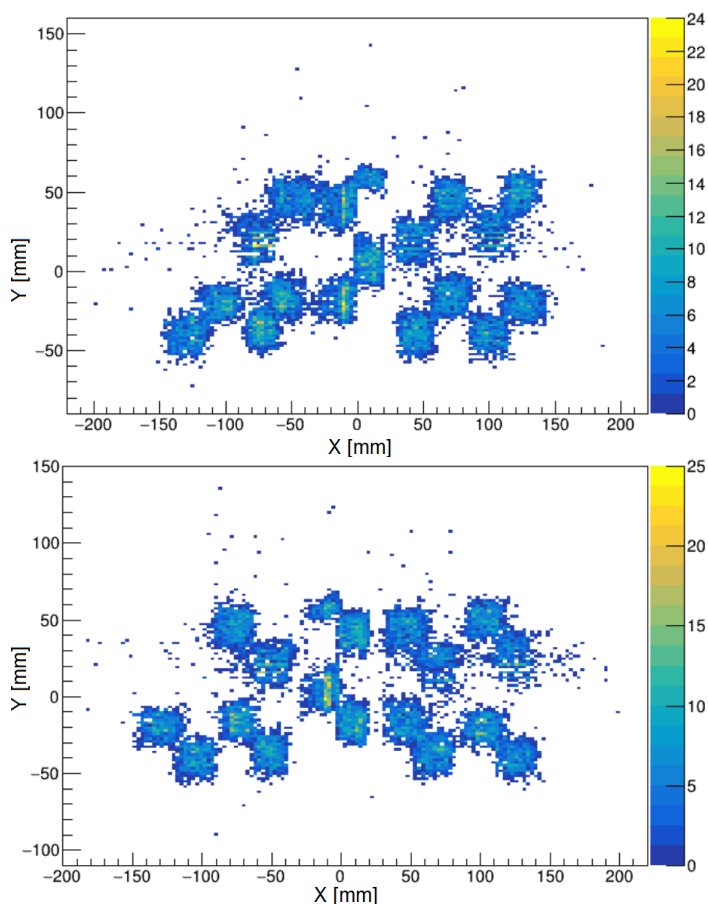


Figure 24: (Top) XZ projection of the Si wall choosing the lower left and upper right quadrants of each Si detector. (Bottom) XZ projection of the Si wall choosing the upper left and lower right quadrants of each Si detector.

- β -delayed charged particle emission - ^{12}N β decay to ^{12}C Hoyle state with subsequent emission of three α -particles.

In this paper we will only focus on describing the experimental procedures for the proton elastic scattering measurements, the experiments that were used as commissioning runs for TexAT and are at the most advanced stages of analysis at this time.

For these experiments, stable beams of ^{12}C and ^6Li were delivered by the K150 cyclotron accelerator at the Texas A&M University Cyclotron Institute.

Tests with stable beam of ^{12}C ions have shown that TexAT can handle up to the 2×10^5 pps with the “fast” gas (methane). For the commissioning experiment the intensity of the stable ^{12}C beam have been reduced to the “safe” level of 10^5 pps .

The ^8B beam was produced using Magnetic Achromat Recoil Separator (MARS) [14] with the reaction $^6\text{Li}(^3\text{He},n)^8\text{B}$. The energy of the ^8B beam was 60 MeV and the intensity was about 1,000 pps. In addition to the regular TexAT detector components/arrays, we installed a thin scintillator, read out by two PMTs, upstream from the TexAT chamber. This detector was used during the run with ^8B beam to count the beam particles before the TexAT setup and help removing the beam contaminants. The scintillator was removed for the run with ^{12}C (the intensity was about 10^5 pps). The PMT signals from the sides of the scintillator were fed to a CFDs with a threshold high enough to trigger only on the ^8B beam particles leaving the beam contaminants, primarily ^3He , below the threshold. The two outputs from the CFD were sent to a logic unit that triggered when both PMT signals were above the threshold. The trigger was then sent to a CAEN VME Scalar unit to count the number of beam ions for overall normalization. The CAEN Scalar was placed on its own data acquisition system separate from the GET electronics. A windowless Ionization Chamber (IC) was also placed inside the TexAT chamber, just after the entrance window to count and identify the beam particles. To trigger the GET electronics, a coincidence between the external signal from the IC and at least one Si detector channel was required (this is the so-called LOL1 mode in GET electronics). This was important to avoid triggering on events associated with ^3He ions in the beam. Unlike ^8B , these light ions do not stop in the gas and trigger the Si detector located on the beam axis, however they do not leave enough energy to trigger the IC, therefore they are vetoed. The digitizer was set to 25 MHz meaning that the waveforms were recorded every 40 ns and the total timeframe window was 20.48 μs (512×40 ns). The system was set to zero suppression mode so that only the channels that fired above the threshold were recorded and written to disk, all the other channels were ignored.

5.1. Beam Particle Identification

In the experiment with the stable beam (^{12}C), there were no beam contaminants. In the rare isotope beam experiment the separation of the ^8B ions from the small contamination, mostly of ^3He , was done using the energy and timing from the ionization chamber. By measuring the energy deposited in the IC and the time relative to the signal in the Si detector, it was possible to cut out the small amount of contamination. Note that the CH_4 gas pressure was set to (435 Torr) so that ^8B ions were stopped long before they could hit the Si detector at zero degrees. Therefore, the correlation between the time of a hit in a Si detector and that of a ^8B ion in the ionization chamber is a signature that a nuclear reaction with ^8B produced a light recoil. Fig. 25 shows the energy deposited in the IC and the time relative to the Si detector. For all “good” events, the ionization chamber

time is mostly determined by the shaping time delay between the ionization chamber signal and that of the Si detectors. We used an external MESYTEC shaper for the ionization chamber signal that was then fed directly into the Gain-2 stage of GET electronics, bypassing the internal AGET preamp, shaper and filter, as described in section 2.5.3. The energy and timing peaks of the ^8B beam in the ionization chamber is clearly seen in Fig. 25. These two quantities were used to make a cut on the events related to ^8B beam.

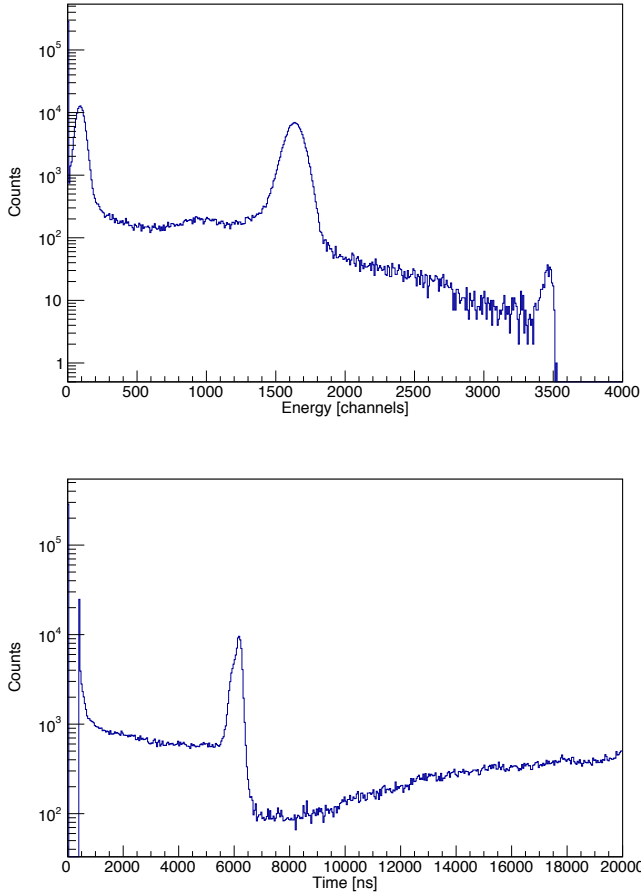


Figure 25: (Top) The energy deposited in the ionization chamber. The ^8B peak is located between channels 1300-1900. (Bottom) The time of the maximum of the ionization chamber. The beam particles corresponding to the Si hit fall between 5400 ns to 6500 ns.

5.2. Tuning of the beam

An important benefit of active target detector is the ability to measure the tracks of the incoming beam ions. This is especially useful when tuning the RIB into the chamber to make sure that it is coming in at the correct angle and stopping in the correct location. Shown in Figure 26 and Figure 27 are the cumulative counts in the central pads during the tuning process. One can see, that the beam stops before the last 1/8th of the pads. Figure 28 is the average specific energy loss in the pads. The figure shows the Bragg curve which occurs as the beam travels further into the chamber and loses more and more

energy, the specific energy loss over each pad becomes larger until it reaches the Bragg Peak around row number 90 (out of 128 total). Note that the radioactive beam of ^8B has much wider profile in the scattering chamber, which is defined by the size of the entrance window, while the profile for the stable ^{12}C beam is rather narrow (see Fig. 27).

Figure 28 is the average specific energy loss in the pads. The figure shows the Bragg curve which occurs as the beam travels further into the chamber and loses more and more energy, the specific energy loss over each pad becomes larger until it reaches the Bragg Peak around row number 90 (out of 128 total).

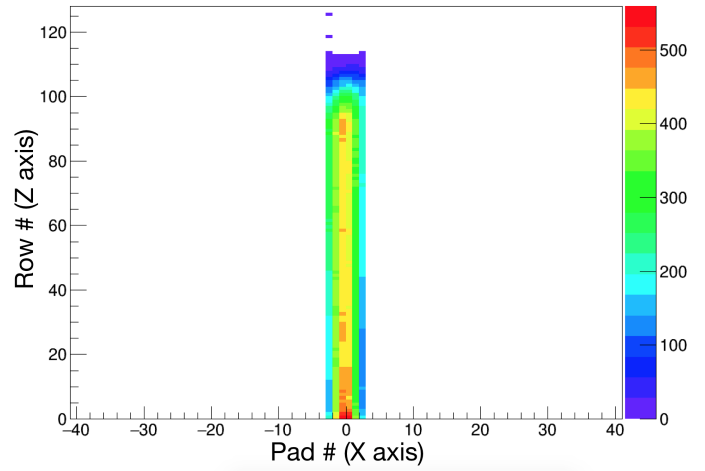


Figure 26: The cumulative counts in the central region of the Micromegas for the ^8B beam. The pressure was adjusted to stop the beam about 1/8th from the end of the Micromegas.

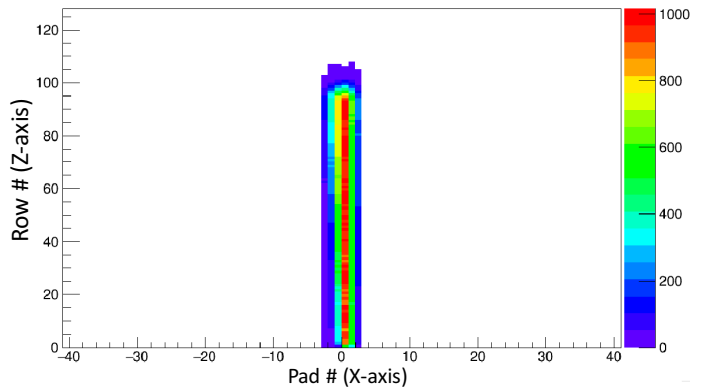


Figure 27: The cumulative counts in the central region of the Micromegas for the ^{12}C beam. The pressure was adjusted to stop the beam about 1/8th from the end of the Micromegas.

5.3. Low and High Gain Areas in the Micromegas Detector

The Micromegas detector was split into effectively two regions: one with low gain and another with high gain. The low gain region consists of the first 7/8th of the central pads in the

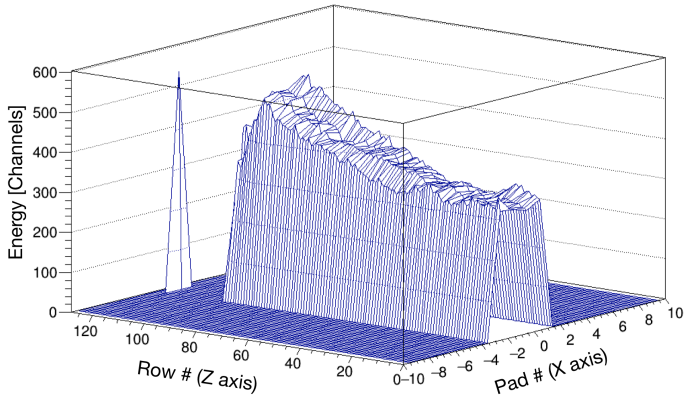


Figure 28: The energy deposited in each of the central region pads. The Bragg peak occurs around row number 90.

beam direction. This low gain region is used to measure the incoming beam particle and the energy deposition along the pads. It had a Micromegas bias of 400 V. The last 1/8th of the central pad region closest to the Si detectors was biased at 600 V and is a high gain region which was used to measure the protons as the beam is stopped before this region. Both side regions were high gain regions biased at 570 V to obtain the proton tracks.

5.4. Selecting Proton Events

To identify proton events, we used the specific energy loss in the high gain regions vs the total energy in the Si and CsI detectors. Since trajectories have variable path length over the active region of Micromegas detector, we use specific energy loss per unit pad for particle ID. The specific energy loss per unit pad for the central detectors plotted against the total energy is shown in Fig. 29. For the side regions, only the energy deposited in the strips are used to get the specific energy loss since the strips run perpendicular to the beam axis. This means that protons traveling in the forward direction will not skip over any strips nor will the geometry of the pad prevent the full measurement of the energy. The specific energy loss per unit pad plotted against total energy in the side region is shown in Fig. 30. As shown in both of these figures, protons are easily identified. The protons that punch-through the Si detectors (> 9 MeV for $700 \mu\text{m}$ of Si) produce a signal in the CsI(Tl) providing additional identification shown in Fig. 31.

The gap in Fig. 29 between ~ 9 and ~ 10 MeV corresponds to the threshold in the CsI detectors. The protons in this energy region do not deposit enough energy in the CsI to be recorded due to the threshold for the CsI(Tl) channels in GET electronics. This threshold can actually be eliminated if complete read-out mode is used in GET, in which case the “threshold” would be defined by the CsI(Tl) noise level. However, it was not done in the commissioning run. Shown in Fig. 31 is the Si energy plotted against the energy deposition in the corresponding CsI(Tl). As shown, we start recording a signal in the CsI

detector when the punch-through protons are only depositing less than 7.5 MeV in the Si detector.

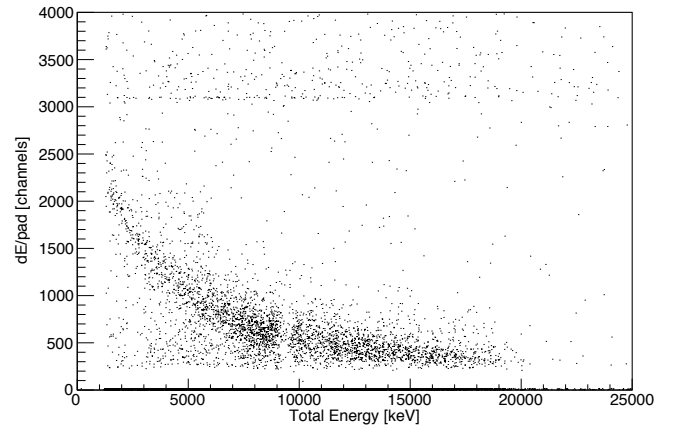


Figure 29: The specific energy loss per unit pad in the central region plotted against the total energy measured in the Si and CsI detector. The energy loss is measured in the last 1/8th in the central pads.

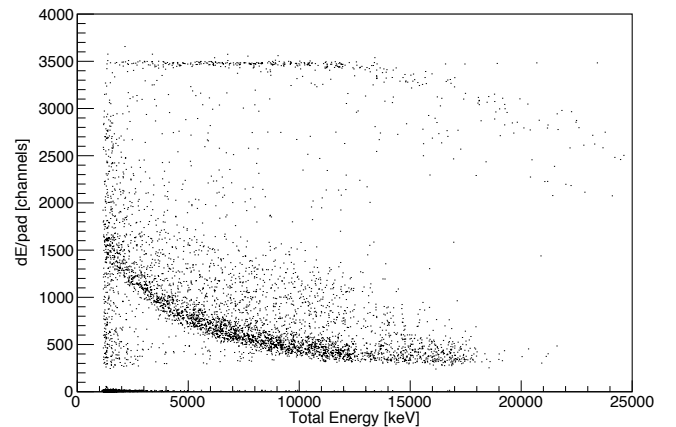


Figure 30: The specific energy loss per unit pad of the strips in the side region plotted against the total energy measured in the Si and CsI detector.

5.5. Identification of inelastic scattering events

The main focus of the commissioning run was measuring the excitation function for ${}^8\text{B}+p$ resonance elastic scattering. However, inelastic scattering events were clearly observed. There are no proton-bound excited states in ${}^8\text{B}$ because its protons decay threshold is located at 137 keV and the first excited states (1^+) is at 770 keV. As a result, any inelastic scattering event will produce two protons and a ${}^7\text{Be}$ recoil (which itself may be in its ground or excited state). Investigating the events with two proton tracks, we can identify these inelastic scattering events.

Using the total energy in the Si and CsI detectors and the Micromegas, we can clearly identify protons that hit one of the Si detectors and triggered the DAQ, but “second” protons produced by an inelastic scattering event do not always hit a Si

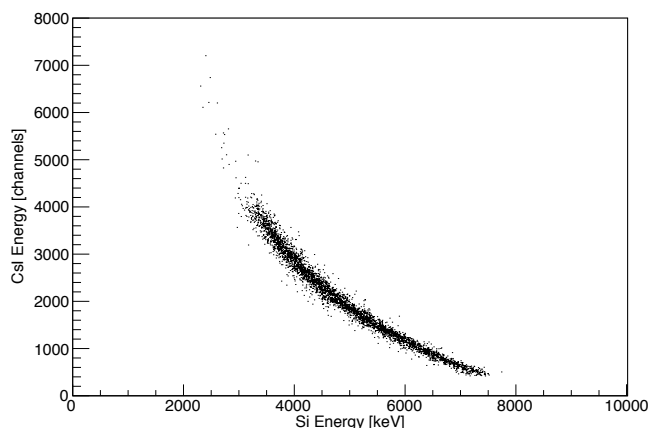


Figure 31: The energy recorded in the CsI detector in channel number plotted against the measured energy (in keV) in the Si detector.

detector. Therefore, we cannot rely on specific energy loss vs the total measured energy and need to identify protons by only using their tracks in the gas. The energy loss of $Z=1$ nuclei is very different from that of heavier recoils (e.g. ${}^7\text{Be}$) and there appears to be no or very few deuterons or tritons produced in the interaction of ${}^8\text{B}$ with the methane gas (see Fig. 29 and 30). So, by comparing specific energy loss per unit pad we can determine if the particle is a heavy recoil or a proton. Examples of protons measured in the side regions and the second proton is measured in the central region (Figure 32) and opposite side region (Figure 33) are shown. By identifying these events, we are able to exclude them from the excitation function for resonance elastic scattering.

5.6. Vertex Reconstruction in the Central Region

The following procedure is used for reconstruction of the event kinematics in the central region. As the ${}^8\text{B}$ beam propagates over the active region of Micromegas, it deposits energy by ionizing gas in the region of central pads. When a reaction occurs over the Micromegas, such as elastic proton scattering, the energy deposition changes. At this reaction point, there is a jump in specific energy loss because the ${}^8\text{B}$ ion transfers a fraction of its energy to the target proton and therefore specific energy loss changes instantaneously at the interaction point. This sudden energy change can be directly observed in the pads as long as the vertex is over the Micromegas. In this measurement, only events below $E_{c.m.} = 3.2$ MeV will have a vertex position over the Micromegas plate. An alternative way to determine the vertex location for central events and for events produced at c.m. energies above 3.2 MeV is to identify the location of the Bragg peak for a heavy recoil. Since the elastically scattered proton events measured in the central detectors travel at angles close to zero degrees, the heavy recoil also travels at angles close to zero (due to momentum conservation). This heavy recoil is then measured completely over the central pad region of the Micromegas. The energy of the heavy recoil produced in the ${}^8\text{B}+p$ elastic scattering depends on the location of the interaction or c.m. energy. These scattered recoils with higher

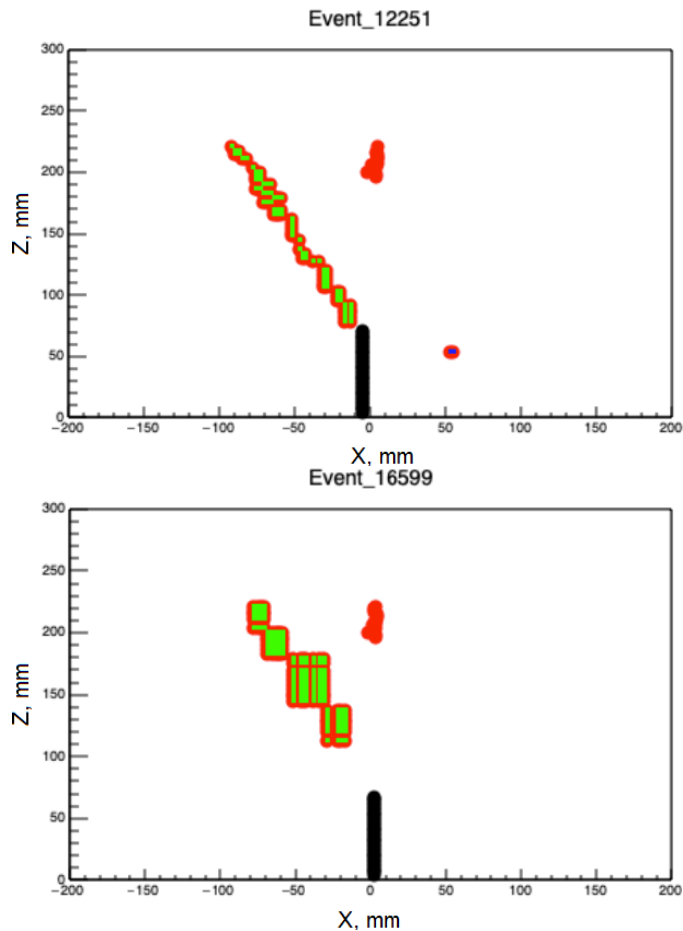


Figure 32: Inelastic events where a proton is measured one side of the Micromegas plate and a proton in the central region.

energies travel further through the gas and the location of the Bragg peak can be measured. Two typical events of this kind are shown in Figure 34. By using kinematics and energy loss, we can formulate a way to relate the maximum energy deposition in the Micromegas with the vertex location. This is used to determine the vertex position for the events that produced a proton in the central region. The vertex position determined this way is plotted against the total energy measured in the Si and CsI in Fig. 35. As expected, the vertex position is further away from the Si detectors (vertex position going further negative) as the total energy becomes higher. This figure demonstrates that vertex location can be reliably identified even if an interaction occurs outside of the active region of Micromegas (negative values along the y axis in Fig. 35).

5.7. Vertex Reconstruction in the Side Regions

Reconstructing the event tracks in the side regions is straightforward. After matching the strips and chains as discussed above, the tracks can then be analyzed using the Hough transform, and traced back to the beam axis to find the vertex location. For events where the vertex is over the Micromegas and the incoming beam is measured, the proton track is traced to the measured incoming beam track. For higher energy events, the beam information is not measured in the Micromegas detector

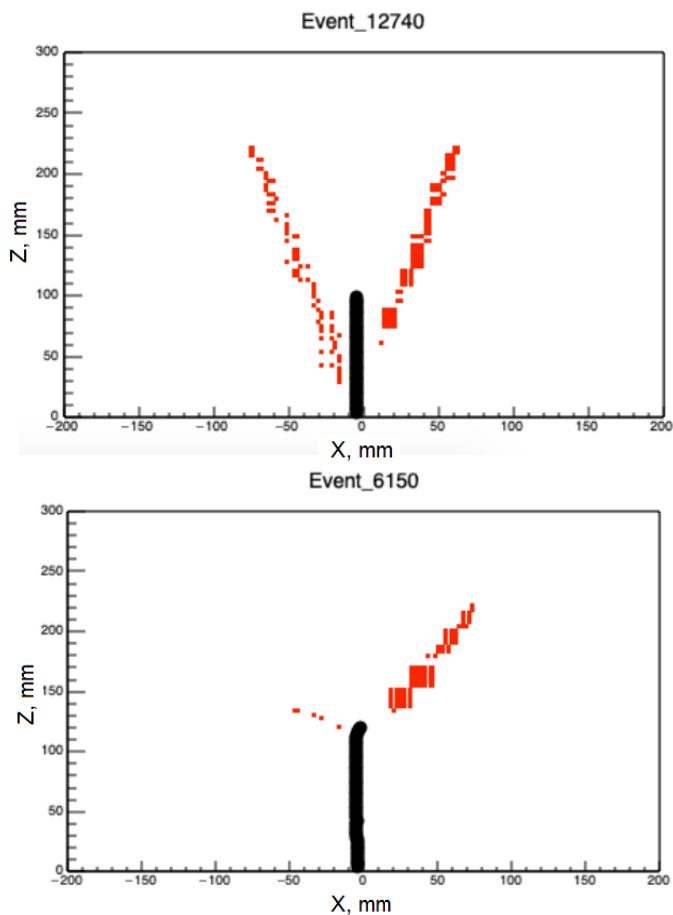


Figure 33: Inelastic events where protons are measured in both sides of the Micromegas plate.

and the proton track is traced back to the “ideal” beam axis. The measured vertex position vs total energy is shown in Fig. 36. As in the case of the central region, elastically scattered events occur further away for high energy events and thus higher c.m. energy events.

6. Conclusion

The new active target detector system - Texas Active Target - has been designed and constructed at the Cyclotron Institute at Texas A&M University. The detector consists of the Time Projection Chamber readout by highly segmented Micromegas detector that provides high gas gains. The TPC is surrounded on five sides by a shell of Si detectors backed by the CsI(Tl) scintillators, readout out by the Si pin-diodes. The detector was first tested with an α -source. The commissioning experiments with the stable ^{12}C beam and the rare isotope ^8B beam were performed. Parameters and properties of TexAT, the TexAT simulation package and simulation results and also track reconstruction procedures are described in this paper. Physics results of the first commissioning run, in which structure of exotic nucleus ^9C was studied, are discussed in [35].

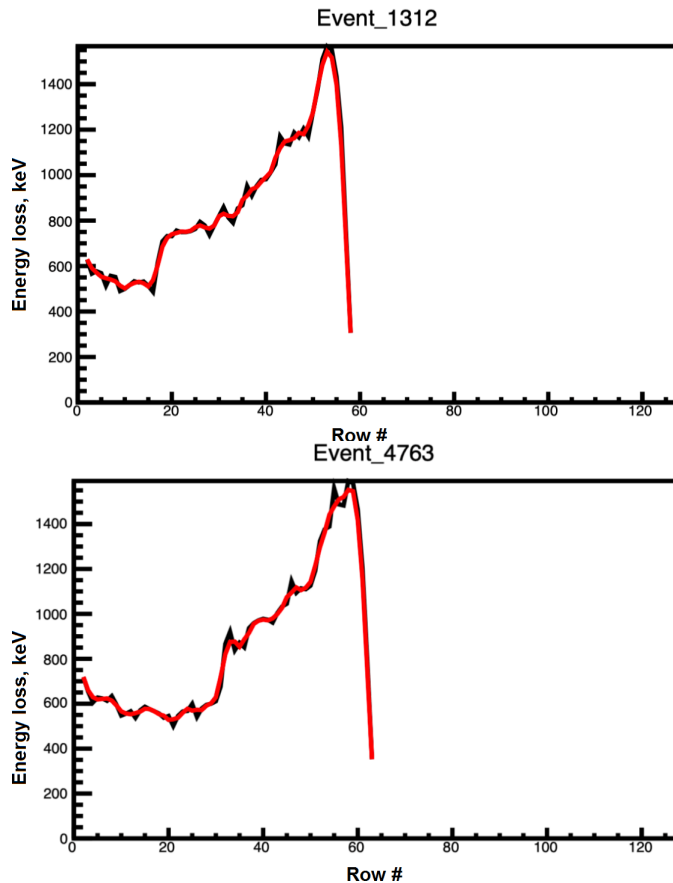


Figure 34: Specific energy loss of the beam and heavy scattered recoil vs row number in Micromegas along the beam axis. Black lines are the raw energy values while the red curve is the running average. (Top) The vertex location is around row 20 while the maximum specific energy loss is around row 50. (Bottom) The vertex location is around row 30 while the maximum specific energy loss is around row 60.

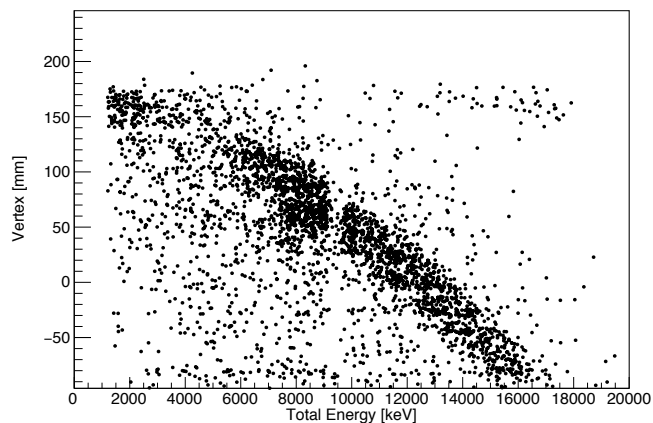


Figure 35: Vertex position vs total energy measured in the Si and CsI detectors for the central forward detectors.

Acknowledgements

TexAT project was supported by the U.S. Department of Energy, Office of Science, Office of Nuclear Science, under Award

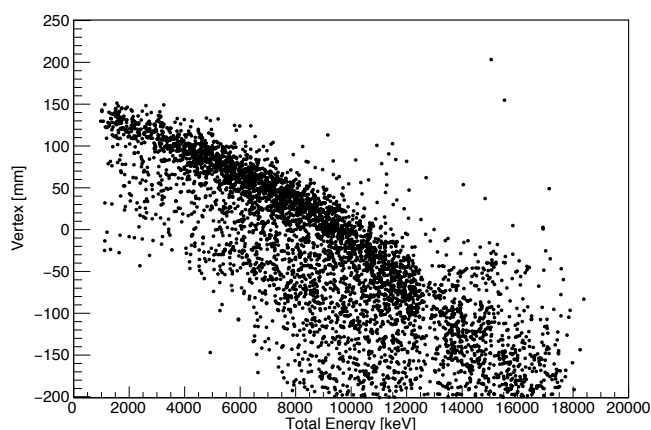


Figure 36: Vertex position vs total energy measured in the Si and CsI detectors for the outside forward detectors.

No. DE-FG02-93ER40773 and by National Nuclear Security Administration through the Center for Excellence in Nuclear Training and University Based Research (CENTAUR) under grant number #de-na0003841. The author G.V.R. is also acknowledge the support of the Welch Foundation (Grant. No. A-1853).

The authors are grateful to Bertrand Mehl, Rui de Oliveira and the detector development team at CERN for their technical support. We thank Yuriy Penionzhkevich (JINR), M.I.Gazizov and detector group at the Institute in Physical-Technical Problems (Dubna, Russia) for their collaboration to develop custom Silicon detectors for TexAT. The authors are deeply thankful the Electronics and Detector Division of IRFU CEA (Saclay): Anvar Shebli, Patrick Baron, Jérôme Pibernat and Patric Sizun for helpful discussions and their support of Micromegas and GET electronics. The authors also grateful to Gilles Wittwer (GANIL) for useful advice.

References

- [1] V. Z. Goldberg and A. E. Pakhomov. *Yad.Fiz.(Rus.)*, **56**:9, 1993.
- [2] A.M. Laird *et al.* *Nuclear Instruments and Methods in Physics Research*, **A573**:306, (2007).
- [3] C. E. Demonchy *et al.* *Nuclear Instruments and Methods in Physics Research*, **A573**:145–148, 2007.
- [4] D. Suzuki *et al.* *Nuclear Instruments and Methods in Physics Research*, **A 691**:39–54, 2012.
- [5] C.F. Ginyer *et al.* *SPIRAL 2 Week*, 2011.
- [6] E. Koshchiy *et al.* *Nuclear Instruments and Methods in Physics Research*, **A 870**:1 – 11, 2017.
- [7] W. Christie *et al.* *Nuclear Instruments and Methods in Physics Research*, **A 255**:466–476, 1987.
- [8] Y. Mizoi *et al.* *Nuclear Instruments and Methods in Physics Research*, **A 431**:112, 1999.
- [9] Ćwiok *et al.* Optical time projection chamber for imaging of two-proton decay of ^{45}Fe nucleus. *IEEE Trans. Nucl. Sci.*, **52**:2895, 2005.
- [10] M. Gai *et al.* An optical readout TPC (O-TPC) for studies in nuclear astrophysics with gamma-ray beams at HIγS. *Jour. Instr.*, **5**:12004, 2010.
- [11] D. Bazin S. Beceiro-Novo, T. Ahn and W. Mittig. Active targets for the study of nuclei far from stability. *Progress in Particle and Nuclear Physics*, **84**:124 – 165, 2015.
- [12] D. González-Díaz *et al.* *Nuclear Instruments and Methods in Physics Research*, **A 878**:200–255, 2018.
- [13] Y. Ayyad *et al.* *The European Physical Journal A*, **54**(10):181, 2018.
- [14] R.E. Tribble, R.H. Burch, and C. A. Gagliardi. MARS: A Momentum Achromat Recoil Separator. *Nuclear Instruments and Methods in Physics Research*, **A285**:441–446, 1989.
- [15] G.A. Shishkina L.A. Grigorieva A.G. Artyukh Yu.G. Teterev L.A. Popeco, I.M. Kotina and Yu.M. Sereda. Thick Si(Li) coaxial detectors for registration of intermediate energy heavy ions. *Nuclear Instruments and Methods in Physics Research*, **A 596**:235–237, 2008.
- [16] Y. Giomataris *et al.* MICROMEGAS: A High granularity position sensitive gaseous detector for high particle flux environments. *Nuclear Instruments and Methods in Physics Research.*, **A 376**:29–35, 1996.
- [17] S. Andriamonje *et al.* *JINST* 5, page P02001, 2010.
- [18] W. Blum and L. Rolandi. *Particle Detection with Drift Chambers*. Springer-Verlag, 1964.
- [19] I. Giomataris *et al.* *Nuclear Instruments and Methods in Physics Research Section A: Accelerators, Spectrometers, Detectors and Associated Equipment*, **560**(2):405 – 408, 2006.
- [20] Heinz Raether. *Electron avalanches and breakdown in gases*. Butterworths, 1964.
- [21] V. Peskov *et al.* The study and optimization of new micropattern gaseous detectors for high-rate applications. *IEEE Trans. Nucl. Sci.*, **48**(4), 2001.
- [22] C. Geuzaine and J.-F. Remacle. GMSH: a three-dimensional finite element mesh generator with built-in pre- and post-processing facilities. *International Journal for Numerical Methods in Engineering*, **79**, pages =, 2009.
- [23] R.Veenhof. GARFIELD: computer code. 1998.
- [24] Elmer: computer code. <http://www.csc.fj/elmer>, 2005.
- [25] MAGBOLTZ: computer code, v.11.4.
- [26] Micron Semiconductor UK, 2018 catalog. <http://www.micronsemiconductor.co.uk>, 2018.
- [27] I.M. Gazizov, I.V. Nikonorov, and A.A. Smirnov. Silicon four-segment charged particle detectors. *EXON2018, Book of Abstracts*, page 113, 2018.
- [28] E.C. Pollacco *et al.* GET: A generic electronics system for TPCs and nuclear physics instrumentation. *Nuclear Instruments and Methods in Physics Research*, **A887**:81 – 93, 2018.
- [29] <https://www.rs-online.com/designspark/pcb-software>, 2017.
- [30] GET-AS-002-0009. *CENBG CNRS Technical Manual*.
- [31] MSCF-16 F Shaping Amplifier. <https://www.mesytec.com/products/nuclear-physics>.
- [32] LM6154 Quad Operational Amplifier. *Texas Instruments Incorporated* (<http://www.ti.com/lit/ds/symlink/lm6152.pdf>).
- [33] S. Agostinelli *et al.* Geant4: A simulation toolkit. *Nuclear Instruments and Methods in Physics Research*, **A 506**:250–303, 2003.
- [34] Richard O. Duda and Peter E. Hart. Use of the hough transformation to detect lines and curves in pictures. *Commun. ACM*, **15**(1):11–15, January 1972.
- [35] J. Hooker *et al.* Structure of ^9C through proton resonance scattering with the texas active target detector. *Phys. Rev. C*, **100**:054618, 2019.